

---

This is an electronic reprint of the original article.  
This reprint may differ from the original in pagination and typographic detail.

Hyypä, Eric; Hyypä, Juha; Hakala, Teemu; Kukko, Antero; Wulder, Michael A.; White, Joanne C.; Pyörälä, Jiri; Yu, Xiaowei; Wang, Yunsheng; Virtanen, Juho Pekka; Pohjavirta, Onni; Liang, Xinlian; Holopainen, Markus; Kaartinen, Harri

## Under-canopy UAV laser scanning for accurate forest field measurements

*Published in:*  
ISPRS Journal of Photogrammetry and Remote Sensing

*DOI:*  
[10.1016/j.isprsjprs.2020.03.021](https://doi.org/10.1016/j.isprsjprs.2020.03.021)

Published: 01/06/2020

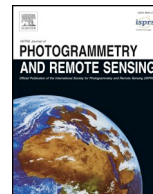
*Document Version*  
Publisher's PDF, also known as Version of record

*Published under the following license:*  
CC BY-NC-ND

*Please cite the original version:*  
Hyypä, E., Hyypä, J., Hakala, T., Kukko, A., Wulder, M. A., White, J. C., Pyörälä, J., Yu, X., Wang, Y., Virtanen, J. P., Pohjavirta, O., Liang, X., Holopainen, M., & Kaartinen, H. (2020). Under-canopy UAV laser scanning for accurate forest field measurements. *ISPRS Journal of Photogrammetry and Remote Sensing*, 164, 41-60. <https://doi.org/10.1016/j.isprsjprs.2020.03.021>

---

This material is protected by copyright and other intellectual property rights, and duplication or sale of all or part of any of the repository collections is not permitted, except that material may be duplicated by you for your research use or educational purposes in electronic or print form. You must obtain permission for any other use. Electronic or print copies may not be offered, whether for sale or otherwise to anyone who is not an authorised user.



## Under-canopy UAV laser scanning for accurate forest field measurements

Eric Hyypä<sup>a</sup>, Juha Hyypä<sup>a,c,\*</sup>, Teemu Hakala<sup>a</sup>, Antero Kukko<sup>a,c</sup>, Michael A. Wulder<sup>b</sup>,  
Joanne C. White<sup>b</sup>, Jiri Pyörälä<sup>a</sup>, Xiaowei Yu<sup>a</sup>, Yunsheng Wang<sup>a</sup>, Juho-Pekka Virtanen<sup>a,c</sup>,  
Onni Pohjavirta<sup>a</sup>, Xinlian Liang<sup>a</sup>, Markus Holopainen<sup>d</sup>, Harri Kaartinen<sup>a,e</sup>

<sup>a</sup> Department of Remote Sensing and Photogrammetry, Finnish Geospatial Research Institute, 02431 Masala, Finland

<sup>b</sup> Canadian Forest Service (Pacific Forestry Centre), Natural Resources Canada, 506 West Burnside Road, Victoria, British Columbia V8Z 1M5, Canada

<sup>c</sup> Department of Built Environment, Aalto University, School of Engineering, P.O. Box 11000, FI-00076 Aalto, Finland

<sup>d</sup> Department of Forest Sciences, University of Helsinki, FI-00014 Helsinki, Finland

<sup>e</sup> Department of Geography and Geology, University of Turku, FI-20014 Turku, Finland

### ARTICLE INFO

#### Keywords:

Airborne laser scanning  
UAV  
Under-canopy flight  
Stem volume  
Stem curve  
SLAM

### ABSTRACT

Surveying and robotic technologies are converging, offering great potential for robotic-assisted data collection and support for labour intensive surveying activities. From a forest monitoring perspective, there are several technological and operational aspects to address concerning under-canopy flying unmanned airborne vehicles (UAV). To demonstrate this emerging technology, we investigated tree detection and stem curve estimation using laser scanning data obtained with an under-canopy flying UAV. To this end, we mounted a Kaarta Stencil-1 laser scanner with an integrated simultaneous localization and mapping (SLAM) system on board an UAV that was manually piloted with the help of video goggles receiving a live video feed from the onboard camera of the UAV. Using the under-canopy flying UAV, we collected SLAM-corrected point cloud data in a boreal forest on two 32 m × 32 m test sites that were characterized as sparse ( $n = 42$  trees) and obstructed ( $n = 43$  trees), respectively. Novel data processing algorithms were applied for the point clouds in order to detect the stems of individual trees and to extract their stem curves and diameters at breast height (DBH). The estimated tree attributes were compared against highly accurate field reference data that was acquired semi-manually with a multi-scan terrestrial laser scanner (TLS). The proposed method succeeded in detecting 93% of the stems in the sparse plot and 84% of the stems in the obstructed plot. In the sparse plot, the DBH and stem curve estimates had a root-mean-squared error (RMSE) of 0.60 cm (2.2%) and 1.2 cm (5.0%), respectively, whereas the corresponding values for the obstructed plot were 0.92 cm (3.1%) and 1.4 cm (5.2%). By combining the stem curves extracted from the under-canopy UAV laser scanning data with tree heights derived from above-canopy UAV laser scanning data, we computed stem volumes for the detected trees with a relative RMSE of 10.1% in both plots. Thus, the combination of under-canopy and above-canopy UAV laser scanning allowed us to extract the stem volumes with an accuracy comparable to the past best studies based on TLS in boreal forest conditions. Since the stems of several spruces located on the test sites suffered from severe occlusion and could not be detected with the stem-based method, we developed a separate work flow capable of detecting trees with occluded stems. The proposed work flow enabled us to detect 98% of trees in the sparse plot and 93% of the trees in the obstructed plot with a 100% correction level in both plots. A key benefit provided by the under-canopy UAV laser scanner is the short period of time required for data collection, currently demonstrated to be much faster than the time required for field measurements and TLS. The quality of the measurements acquired with the under-canopy flying UAV combined with the demonstrated efficiency indicates operational potential for supporting fast and accurate forest resource inventories.

\* Corresponding author at: Department of Remote Sensing and Photogrammetry, Finnish Geospatial Research Institute, 02431 Masala, Finland.

E-mail addresses: [eric.hyypa@gmail.com](mailto:eric.hyypa@gmail.com) (E. Hyypä), [juha.coelars@gmail.com](mailto:juha.coelars@gmail.com) (J. Hyypä), [teemu.hakala@nls.fi](mailto:teemu.hakala@nls.fi) (T. Hakala), [antero.kukko@nls.fi](mailto:antero.kukko@nls.fi) (A. Kukko), [mike.wulder@canada.ca](mailto:mike.wulder@canada.ca) (M.A. Wulder), [joanne.white@canada.ca](mailto:joanne.white@canada.ca) (J.C. White), [jiri.pyoralahelsinki.fi](mailto:jiri.pyoralahelsinki.fi) (J. Pyörälä), [xiaowei.yu@nls.fi](mailto:xiaowei.yu@nls.fi) (X. Yu), [yunsheng.wang@nls.fi](mailto:yunsheng.wang@nls.fi) (Y. Wang), [juho-pekka.virtanen@aalto.fi](mailto:juho-pekka.virtanen@aalto.fi) (J.-P. Virtanen), [onni.pohjavirta@aalto.fi](mailto:onni.pohjavirta@aalto.fi) (O. Pohjavirta), [xinlian.liang@nls.fi](mailto:xinlian.liang@nls.fi) (X. Liang), [markus.holopainen@helsinki.fi](mailto:markus.holopainen@helsinki.fi) (M. Holopainen), [harri.kaartinen@nls.fi](mailto:harri.kaartinen@nls.fi) (H. Kaartinen).

<https://doi.org/10.1016/j.isprsjprs.2020.03.021>

Received 21 December 2019; Received in revised form 29 March 2020; Accepted 31 March 2020

0924-2716/ © 2020 The Authors. Published by Elsevier B.V. on behalf of International Society for Photogrammetry and Remote Sensing, Inc. (ISPRS). This is an open access article under the CC BY-NC-ND license (<http://creativecommons.org/licenses/by-nc-nd/4.0/>).

## 1. Introduction

Due to the growing demand of forests for various ecosystem services, there is an increasing need for accurate and fast forest field inventories. Even though the technological aspects of forest inventories have been advanced remarkably using remote sensing during the last decades, operational inventories still rely mainly on manual measurements of field plots. These field plots are used for the calibration of airborne or space-borne remote sensing data using the relationship between these data and the forest attributes measured in the plot. Automation of the field plot collection is needed due to the high cost and labour related to manual measurements.

Conventional field plot measurements are implemented using calipers, measuring tapes and hypsometers. Moreover, the consistency and accuracy of these measurements is variable (Luoma et al., 2017; Wang et al., 2019a). Some of the most common plot level metrics for individual trees include diameter at breast height (DBH) and tree height (H), which inform about the maturity of wood and the share of structural timber. Another common stem metric is the stem curve or taper (the rate at which stem diameter changes as the function of stem height) that relates to growth rate, earlywood/latewood ratio and maturity of wood, as described in Lindström (2007). These metrics together with species information are essential for forest industry. Stem volume is, then, typically derived using an allometric model based on a measurement of the DBH, possibly the diameter at a height of 6 m, and the tree height. Such an approach leads to an accuracy ranging from 10% to 15% for the individual stem volume. This accuracy level has been reached with remote sensing techniques only when using multi-scan terrestrial laser scanning and the best state-of-the-art algorithms (Liang et al., 2018a). The main drawbacks of TLS are e.g.: (1) the occlusion problem hindering the completeness of tree digitization and (2) the limited efficiency and mobility of the TLS system setup (Wang et al., 2019b). Thus, new methods for field measurements need to be developed.

In this paper, we propose to employ under-canopy unmanned airborne vehicle (UAV) laser scanning to pave the way for autonomous forest inventory as introduced by Jaakkola et al. (2017). As a relatively new technology, the history of using under-canopy UAV laser scanning for making direct DBH measurements is short. Vandapel et al. (2005) initially proposed the idea of a UAV flying under the canopy by computing a network of free space bubbles forming safe paths within environments cluttered with tree trunks, branches, and dense foliage measured earlier from above the canopy. Aiming to reduce operator dependencies, Vian and Przybylko (2012) patented a remote sensing sensor system associated with the unmanned aerial vehicle capable to generate obstacle information and tree measurement information. Chisholm et al. (2013) implemented a UAV lidar for forest surveys along the road side to measure tree diameters directly, flying the UAV around a 20 m × 20 m patch of roadside trees. They developed post-processing software to estimate the DBH of 12 trees that were detected by the LiDAR resulting in 73% of trees (DBH > 20 cm) detected and measured with a relative root-mean-squared error (RMSE) of 25.1% (about 10 cm).

Thus far, almost all of the research on UAV laser scanning has concerned above-canopy flying UAVs. First miniUAV-based laser scanners were developed in early 2010. Jaakkola et al. (2010) designed the first mini-UAV laser scanner and assessed the accuracy and feasibility of the method for tree measurements. They found that the standard deviation of individual tree heights was approximately 30 cm. They also demonstrated a method to derive the biomass change of coniferous trees from a multitemporal point cloud with a coefficient of determination of 0.92. Wallace et al. (2012) employed a similar system, and concluded that the standard deviation of tree height measurements decreased from 0.26 m to 0.15 m, when the point density was increased from 8 pts/m<sup>2</sup> to approximately 50 pts/m<sup>2</sup>. In Wallace et al. (2014), above-canopy UAV laser scanning data was used to correctly detect

91% of the trees. Additionally, they were able to derive the crown area with an error below 3.3 m<sup>2</sup> for approximately 90% of the trees.

Unfortunately, DBH, unlike the crown size or tree height, is difficult to measure directly from above the canopy with a good accuracy, thus necessitating the use of functions that relate crown size and tree height to DBH (e.g. Hyypä et al., 2001). However, there are a few studies that have measured DBH directly from dense airborne laser scanning (ALS) point clouds collected from above the canopy. Jaakkola et al. (2017) were the first to directly measure DBH directly from above the canopy, followed by Brede et al. (2017) and Wieser et al. (2017). Using a Velodyne-16 sensor, Jaakkola et al. (2017) obtained 6.5 cm as the RMSE of the direct DBH measurement. Using RiCOPTER, Brede et al. (2017) obtained 4.2 cm and Wieser et al. (2017) 2 cm for the RMSE of DBH. Harikumar et al. (2017) used long-range airborne laser scanner data and found 5.7 cm as the RMSE of the stem diameters.

Obtaining high-quality direct measurements from the stems using above-canopy laser scanning requires expensive sensors, since the point spacing and beam size should be small to allow for the accurate measurement of the stem, but both of these properties deteriorate as a function of range. Such sensors and platforms, such as RiCOPTER, are currently at the level of 300 k€ in costs, whereas under-canopy laser scanners can be based on those that are to be developed for autonomous driving (e.g. Velodyne VLP-16 laser scanner) and currently cost approximately few thousands of euros. These sensors are expected to drop in price to some hundreds of euros, as a result of mass production.

However, under-canopy UAV laser scanning suffers from the low quality of the GNSS (Global Navigation Satellite System) signal and therefore, accurate positioning of the scanner requires the use of simultaneous localization and mapping (SLAM) algorithm as in the case of ground-based mobile laser scanning techniques (e.g., Tang et al., 2015; Qian et al., 2017; Kukko et al., 2017; Pierzchała et al., 2018). Nowadays, SLAM technology has already been integrated into some commercial laser scanners, such as Kaarta Stencil, GeoSLAM Horizon and Zebedee systems. In recent years, several innovative methods have been proposed in order to further reduce the effects of positioning errors affecting SLAM corrected point clouds. Liang et al. (2014c) used a multipass-corridor-mapping method to alleviate the problems arising from the positioning errors propagating in time. Forsman et al. (2016) determined the DBH of trees by extracting consecutive points forming circular arcs instead of analyzing the point cloud as a whole. Čerňava et al. (2019) used the iterative closest point algorithm to match points reflected from the same tree at different times in order to improve the modeling accuracy of the stems. Holmgren et al. (2019) applied tree spine calibration based on the Kalman filter to reduce the distortion of the stems in the point cloud. Recently, Hyypä et al. (2020) showed that an arc-based stem detection algorithm combined with an iterative arc matching algorithm could be used to extract the stem curves of trees from an MLS point cloud with an RMSE of approximately 5% in easy and medium-difficult boreal forests.

In this paper, we used an under-canopy flying UAV laser scanner with an integrated SLAM system to collect high-quality point cloud data for two test sites located in the boreal forest zone. The under-canopy flying UAV was manually piloted with the help of video goggles receiving a live video feed from a camera mounted on the UAV. The objective of this paper is to demonstrate that under-canopy UAV laser scanning can generate high quality point clouds, from which automatic algorithms can derive the stem curves of trees with a high precision (RMSE ≈ 5%) in boreal forest stands classified as sparse and obstructed. Additionally, we demonstrate that the stem volume of individual trees can be estimated with a high precision (RMSE ≈ 5%) by combining the stem curves extracted from the under-canopy UAV laser scanning data and tree heights extracted from above-canopy UAV laser scanning data. We compared the estimated individual stem curves and volumes against highly accurate field reference data acquired semi-manually with multi-scan TLS. Furthermore, we describe a novel tree detection algorithm that enables the detection of trees whose stems are

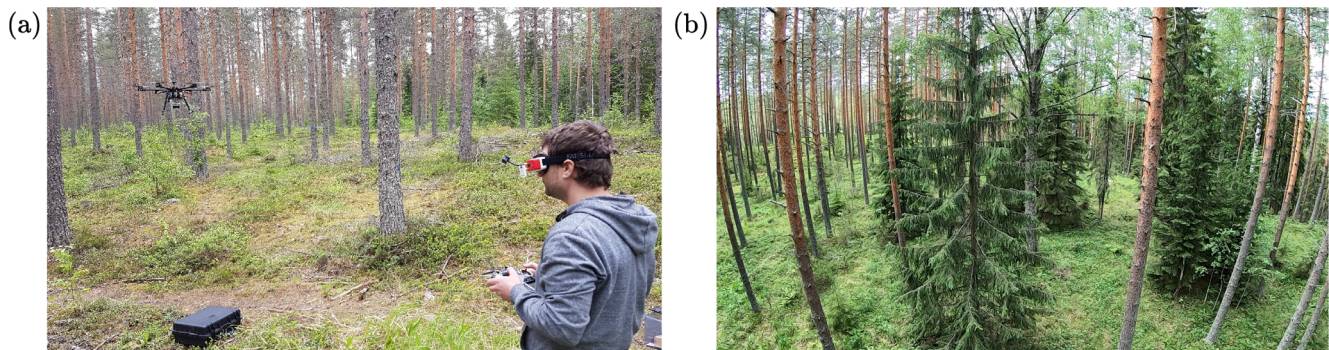


Fig. 1. (a) An overview of the sparse plot. The figure also shows the UAV that was manually piloted with the help of video goggles receiving a live video feed from the onboard camera of the UAV. (b) The obstructed plot viewed from the onboard camera of the UAV.

severely occluded. In this research, we also discuss the future opportunities for robotic-assisted surveying, with insights expected beyond the forest measurement example presented here.

## 2. Materials and methods

### 2.1. Test sites

In this study, the under-canopy and above-canopy UAV measurements were carried out on two 32 m × 32 m test sites both located in a boreal forest in Evo, Finland (61.19°N, 25.11°E) and illustrated in Figs. 1(a) and (b). These two test sites were employed to (1) test the feasibility of the concept in varied forest stand conditions; and (2) to include a sufficient number of trees for verification of the developed methods. The complexity of the forest on the two test sites had been assessed *a priori* by experts based on the stem density of the plot, the species composition of the vegetation, the visibility of the stems, and the size distribution of trees, following the approach described, e.g., in Liang et al. (2018b).

The first test site had been classified as a sparse plot (called as “easy plot” in Liang et al., 2018b) due to a low stem density, the sparsity of understory vegetation, and the homogeneity of trees. On this test site, over 90% of the 42 trees are pines (*Pinus sylvestris* L.), whereas the remaining three trees are spruces (*Picea abies* L. Karst.). The second, obstructed test site belongs to the difficulty category “medium” according to Liang et al. (2018b) due to moderate understory vegetation, larger variations in the tree sizes and a more varied tree species distribution as can be seen from Table 1. In addition to pines, the obstructed plot includes 5 birches (*Betula pendula* Roth and *Betula pubescens* Ehrh.) with somewhat non-circular stems and 8 spruces that are characterized by a poor stem visibility due to the high number of branches. More detailed statistics of the test sites are provided in Table 1.

### 2.2. Data acquisition using under-canopy UAV laser scanning

A hexacopter drone, Tarot 960 (Tarot Aviation Technology co., LTD, Wenzhou, China), with a payload capacity of 4 kg and a flight time of 20 min was used for the under-canopy UAV flights carried out in early

Table 1

Descriptive statistics of the two forest stands including trees exceeding 5 cm in DBH. The standard deviations of tree height and DBH are reported within the parenthesis.

Test site	Number of trees	Stem density (stems/ha)	Average DBH (cm)	Average tree height (m)	Tree species distribution		
					Pines (%)	Spruces (%)	Birches (%)
Sparse	42	410	25.9 (±5.2)	21.4 (±2.8)	92.9	7.1	0.0
Obstructed	43	420	27.0 (±10.1)	22.2 (±6.0)	69.8	18.6	11.6

June 2019. The UAV used Pixhawk autopilot with Arducopter firmware. The laser scanner was mounted horizontally to the bottom of the UAV with only some occlusion from the vertical landing gear tubes at the sides of the UAV. For piloting the UAV, an analogue video camera and a 5.8 GHz radio transmitter were installed to the front of the UAV. The video was transmitted to video goggles and the UAV was manually piloted using the live video feed from the onboard camera. This type of piloting is called first person view (FPV) flying. A spotter was present during the flights next to the pilot to monitor the surroundings as the pilot had no direct line of sight with the UAV. During the flights the study area was covered as well as possible, as straight flight lines were not possible and some areas were impassable with the UAV. The flight together with the on-site preparations lasted for approximately 10–15 min on each of the sample plots. The trajectory of the UAV flight on the sparse test site is illustrated in Fig. 2.

The scanner attached to the UAV was a Kaarta Stencil SLAM-system (Kaarta, Pittsburgh, Pennsylvania, USA) based on a Velodyne VLP-16 laser scanner (Velodyne Lidar, San Jose, California, USA) mounted on an aluminium platform together with the operating computer. The laser scanner ( $\lambda = 903$  nm) had 16 laser profiles with an angular resolution of 2 degrees resulting in a vertical field of view of  $\pm 15$  degrees. Due to the rotation of the laser profiles, the scanner had a horizontal field of view of 360 degrees. According to the manufacturer, the maximum range of the scanner is 100 meters and the ranging accuracy is  $\pm 3$  cm. Due to the long range of the scanner, the obtained point cloud covered an area larger than the 32 m × 32 m test site. The resulting point density within the actual plot was  $1.3 \times 10^4$  pts/m<sup>2</sup> in the sparse plot and  $2.4 \times 10^4$  pts/m<sup>2</sup> in the obstructed plot. The sampling frequency of the scanner (300 kHz) was used to obtain approximate time stamps for each of the points in the point cloud. The settings for data collection and SLAM processing were set according to the manufacturer’s recommendations in a forest environment. Fig. 3(a) illustrates the raw point cloud of the obstructed plot obtained with the laser scanner mounted on the under-canopy flying UAV. Note that the tree tops are not accurately captured in the point cloud due to the narrow field of view of the scanner.

### 2.3. Data acquisition using above-canopy UAV laser scanning

In order to conduct high quality tree height measurements needed

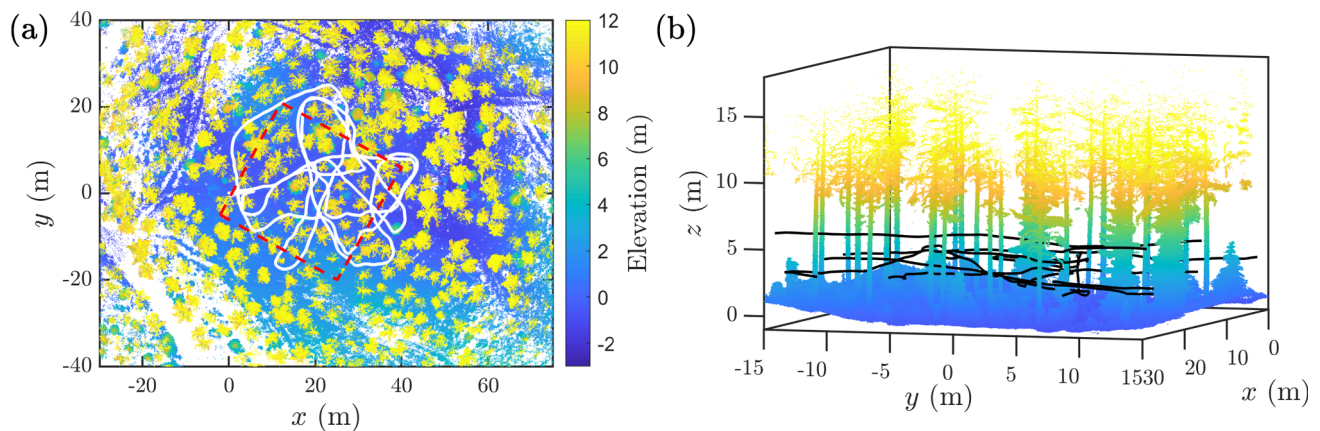


Fig. 2. (a) Top view of the trajectory of the under-canopy flying UAV (white line) in the sparse plot. The red dashed line shows the boundary of the 32 m × 32 m test site. (b) Side view of the trajectory (black line) in the sparse plot.

for the stem volume computation, we analyzed additional above-canopy UAV laser scanning measurements collected on the same sites. The above-canopy flights were conducted in September 2017, using the RiCOPTER (Riegl GmbH, Horn, Austria) that was equipped with a Vux-1 (Riegl GmbH, Horn, Austria) UAV LiDAR sensor, an inertial measurement unit (IMU) and a GNSS unit. Thus, there was practically one growing season difference between the above-canopy and under-canopy UAV flights. The data was collected at 50 meters above the ground with multiple overflights from different directions. The scanner was operated with 550 kHz laser pulse rate, 120 degrees field-of-view and 106 scan lines per second, resulting in 0.07 degrees measurement resolution in each line. The typical flying speed was 2–4 m/s, which produced a point spacing of 3.3 cm in a scan line and 2–4 cm in the flying direction on the ground.

Due to the high overlap between different flight lines, the point density increased vastly, resulting in point densities in the range of 4000–18,000 points/m<sup>2</sup> at the sample plots. As can be seen from Fig. 3(b), the point cloud acquired using the above-canopy flying UAV captures accurately both the canopy and the ground level, which enables measuring the tree heights with a high precision. Note that the geometric accuracy of the stems in the data was limited due to the occlusion from the upper canopies. As was reported in Liang et al. (2019), the relative RMSE of the DBH derived from such data was as high as 15% in sparse forest plots.

#### 2.4. Reference measurements of stem curve, tree height and stem volume

In order to obtain accurate reference measurements of the stem curves, a multi-scan TLS point cloud of the test sites was analyzed semi-manually. The TLS measurements had been carried out in the summer of 2014. To extract the stem curves, trees were first manually detected from the multi-scan TLS point cloud. Subsequently, circles were fitted to the manually identified stem points at the heights of 0.65 m, 1.3 m, 2.0 m, 3.0 m and thereafter at every subsequent 1 m up to the maximum measured height of the stem. Note that this process yields as precise reference results for the stem diameter at different heights as is possible without using a logging machine that requires damaging and felling the trees (see, e.g. Liang et al., 2014b).

Since the multi-scan TLS measurements were conducted in 2014, i.e., 5 years before the under-canopy UAV measurements, the reference stem curves had to be calibrated by performing field measurements in the summer of 2019 in order to account for the 5-year growth of the trees. By measuring the diameter at breast height for each tree with a tape measure, we were able to determine an approximation for the tree specific diameter growth during the 5-year period. In the calibrated stem curves, the 5-year growth of the DBH was added to the reference diameters at all heights. Naturally, this calibration process did not take into account a possible change in the shape of the tree. The tree diameters had grown on average by roughly 1.8 cm during the period.

The reference tree heights required for the stem volume computation were obtained with ordinary field measurements conducted using a

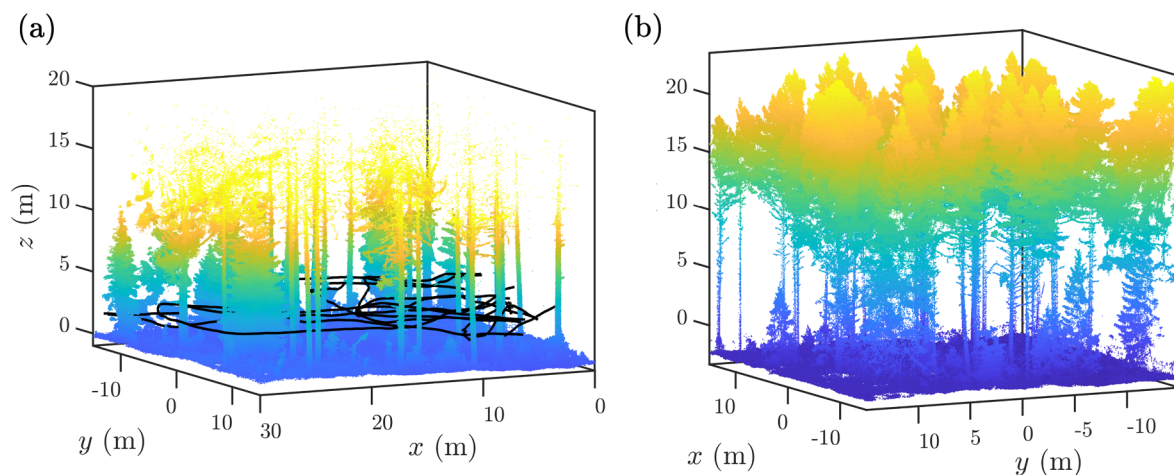


Fig. 3. (a) SLAM-corrected point cloud of the obstructed plot obtained using the laser scanner mounted on the under-canopy flying UAV. The solid black line illustrates the trajectory of the UAV. (b) Raw point cloud of the obstructed plot acquired with the scanner mounted on the above-canopy flying UAV.

hypsoneter. These measurements were carried out in the summer of 2019. The reference values for the stem volume were then estimated by utilizing both the reference stem curves and the reference heights in a manner similar to that proposed by Hyypä et al. (2020). First, we fitted a parabolic function

$$R_1(z) = a_1(h - z)^2 + a_2(h - z), \quad (1)$$

and a square root function

$$R_2(z) = b_1 \sqrt{h - z} \quad (2)$$

to the reference radii  $R$  at different heights  $z$ . Note that the fitting functions equal zero at the reference height  $h$  of the tree. After determining the parameters  $\{a_1, a_2, b_1\}$  by ordinary least squares regression, the reference stem volume  $V$  was determined by computing the average of the volume estimates provided by the fits as

$$V = \frac{\pi}{2} \left( \int_0^h R_1(z)^2 dz + \int_0^h R_2(z)^2 dz \right) = \pi \int_0^h R_{\text{eff}}(z)^2 dz, \quad (3)$$

where  $R_{\text{eff}}(z) = \sqrt{R_1(z)^2 + R_2(z)^2} / 2$  is the effective radius corresponding to the volume estimate.

This process was used to determine the reference stem volumes since the fitting functions approximate well the shape of the stem curve at heights above the reference measurements. Importantly, the risk of over-fitting is also small despite the missing diameter measurements close to the tree top thanks to the low number of fitting parameters. In Hyypä et al. (2020), it was estimated that this fitting process can estimate the total stem volume with an error below 5%.

### 3. Applied algorithms for the extraction of DBH, stem curve and stem volume

In this section, we present the algorithms that were employed to extract the DBH and stem curve for trees with partly visible stems from the point cloud obtained with under-canopy UAV laser scanning. The algorithm used for robust stem point detection is completely novel, but the arc matching process used for improving the stem modeling accuracy is based on the workflow proposed by Hyypä et al. (2020). Additionally, we propose a novel algorithm for tree detection that is capable of detecting trees with both visible and occluded stems. Finally, we describe a method used to extract the tree heights from the above-canopy UAV laser scanning data and the process that was used to predict the stem volumes based on the stem curve and tree height information. Note that all the methods presented in the following subsections are automatic and do not require any manual processing of the data apart from the heuristic choice of the parameters of the algorithms. See Fig. 4 for a simplified flow chart of the data processing workflow.

We stress that the parameters of the algorithm have not been optimized but instead they have been chosen heuristically based on, e.g., the point density of the point clouds, the ranging accuracy of the scanner, the average diameter of the trees on the test sites, and the desired quality of the arcs to be extracted. In appendix A, we present a sensitivity analysis for the parameters of the algorithm showing that the algorithm is robust against reasonable changes in the parameter values.

#### 3.1. Digital terrain model and preliminary segmentation

As a pre-processing step, we removed clearly outlying data points in the  $z$  direction from both above and below the point cloud using a simple point density criterion. Subsequently, a digital terrain model (DTM) was generated for each of the test sites. The DTM creation began by dividing the  $xy$  plane into pixels of size  $50 \text{ cm} \times 50 \text{ cm}$  for the sparse test site and into pixels of size  $70 \text{ cm} \times 70 \text{ cm}$  for the obstructed test site. Furthermore, the  $z$  direction was divided into height intervals of width  $1.0 \text{ m}$  for both the sparse and the obstructed site. For each pixel, we computed the total number of points within each height interval. Subsequently, the ground level in each pixel was obtained by

computing the average  $z$  coordinate of the data points located in the lowest height interval containing at least 1% of the total number of points within the pixel. The final DTM was obtained after Gaussian smoothing. Using the DTM, the  $z$  coordinates of all the data points were normalized by subtracting away the ground level at the point location.

Subsequently, we divided the point cloud into smaller segments by applying the watershed algorithm for the canopy height model that had been generated based on the maximum  $z$  coordinates within each pixel. This preliminary segmentation was performed in order to markedly reduce the running time of the clustering algorithm used for the stem detection described in the next section. Additionally, we used a few of the watershed segments to fine-tune the heuristically chosen parameter values of the stem curve extraction algorithm.

#### 3.2. Algorithm for stem detection and stem curve extraction from the under-canopy UAV laser scanning data

Our first goal in the stem curve extraction algorithm was to identify points that had been reflected from the tree trunks. When identifying stem points, we needed to take into account the positioning errors that resulted from the movement of the laser scanner. Namely, we observed that the positioning error of the scanner was still on the order of  $10 \text{ cm}$  or above although we used the integrated, high-quality SLAM-system of the Kaarta Stencil-1 scanner in the data collection.

To overcome the problems arising from the positioning errors, we used an arc-based approach together with an arc matching algorithm that was first proposed by Hyypä et al. (2020). Since the study by Hyypä et al. (2020) was based on a 2D laser scanner, we had to develop a novel and robust algorithm capable of finding arcs corresponding to stems from a point cloud collected with a 3D laser scanner. As a first step of our arc finding algorithms, we used a time-based clustering method that resembles the approach adopted by Černáva et al. (2019). Namely, we divided the time into short intervals and grouped the data points based on their time stamps. The duration of each time interval was chosen to be  $1 \text{ s}$  since the SLAM-system was observed to work very precisely at this time scale. Additionally, we divided the  $z$  axis into height intervals with a width of  $0.4 \text{ m}$  starting from  $1 \text{ m}$  above the ground. Note that we only considered points that were located at least  $1 \text{ m}$  above the ground level in order to avoid points reflected from the understory vegetation or ground.

Then, we applied the following arc extraction procedure for data points belonging to a certain height and time interval. First, we projected the data points to the  $xy$  plane and applied a well-optimized implementation of the density-based clustering for applications with noise (DBSCAN) (Ester et al., 1996) in order to group the points into clusters. In the DBSCAN clustering, a point was regarded as a core point of a cluster if there were at least  $\text{minPts}_1 = 12$  points within a range of  $\epsilon_1 = 7.5 \text{ cm}$  from the point. The point number threshold  $\text{minPts}_1$  was chosen based on the typical DBH of trees and the quality criteria used in the arc finding (see the end of this subsection). In order to achieve fast running times, we used a well-parallelized quadratic implementation of DBSCAN for small data sets with less than 3000 points, and a sub-quadratic implementation based on kd trees for large data sets. Fig. 5(a) illustrates the effect of DBSCAN clustering for a simulated data set.

To further filter out noise points present in the clusters, we applied robust circle fitting using the random sample consensus (RANSAC) framework (Fischler and Bolles, 1981) for each of the clusters separately. For each cluster, we randomly chose three points through which a circle was fitted. After fitting the circle we computed the number of inliers, i.e., the number of points located at most at a distance of  $d_{\text{in}} = 3.0 \text{ cm}$  from the fitted circle. The process was repeated for several times and the circular fit with the most inliers was regarded as the final fit. If the number of inliers corresponding to the final fit was at least  $\eta_{\text{in}} = 70\%$  of all the points in the cluster, the fit was accepted and the outlying points were deleted from the cluster. Otherwise, the fit and the corresponding cluster were rejected from further analysis. Note that the

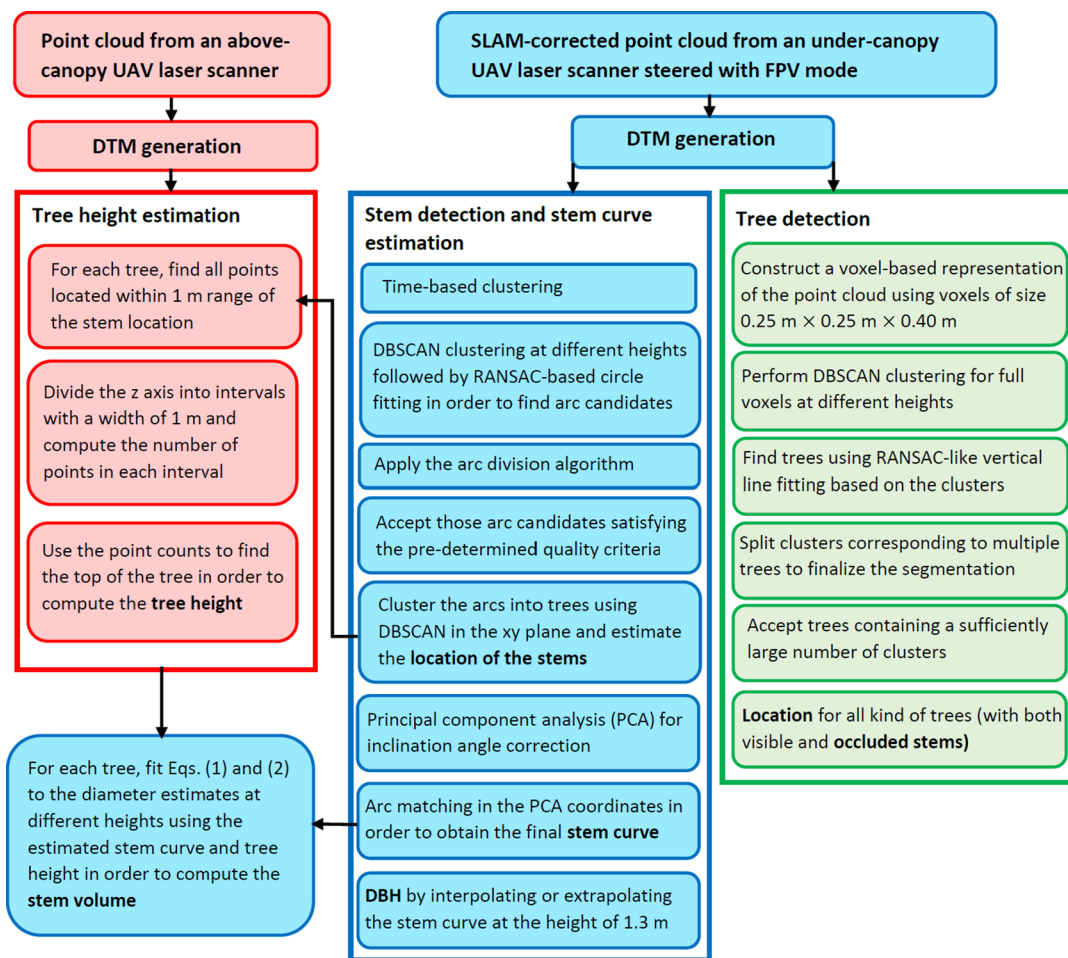


Fig. 4. Flow chart illustrating the steps of the data processing workflow.

number of iterations in the RANSAC loop was obtained with the following equation

$$N_{\text{RANSAC}} = \frac{\log(1 - 0.99)}{\log(1 - \eta_{\text{in}}^3)}, \quad (4)$$

where log refers to the natural logarithm. This number of RANSAC iterations ensured that we obtained at least one set of 3 inlying

points with a probability of 99% assuming that the inlier ratio equaled  $\eta_{\text{in}}$ . The effect of the RANSAC-based circle fitting and outlier removal is illustrated in Fig. 5(b).

Importantly, it is possible that there still remained noise points close to the edges of the clusters even after performing the DBSCAN algorithm and the RANSAC-based circle fitting procedure as illustrated in Fig. 6(a). Such noise points can arise from the presence of branches or

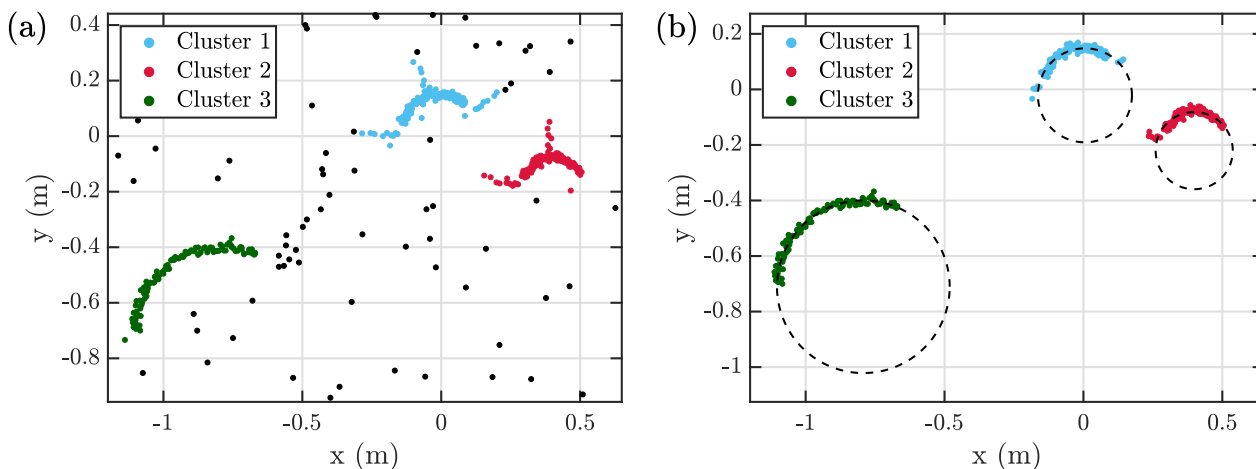
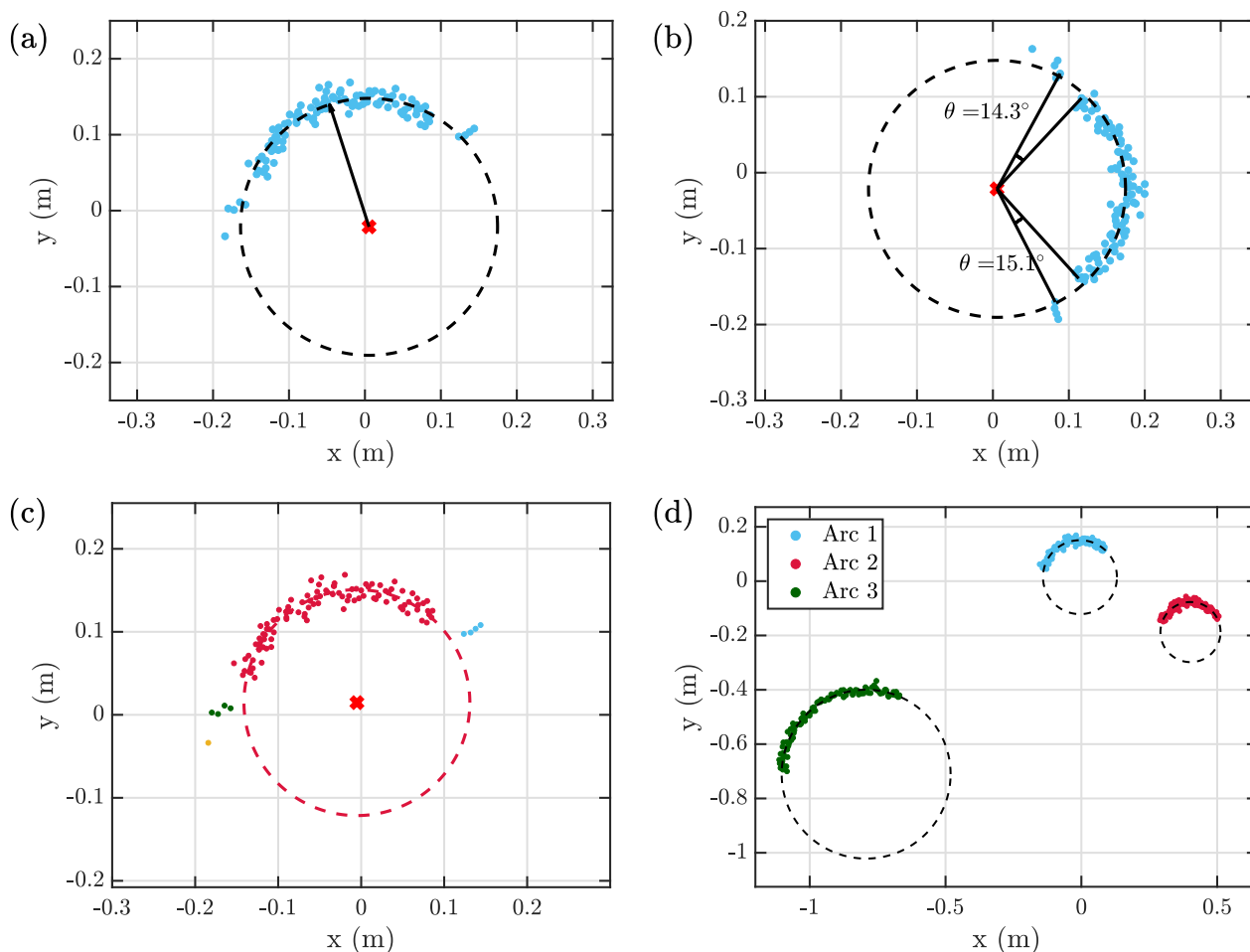


Fig. 5. (a) A few arcs and some noise points used to illustrate the working principle of the arc extraction algorithm that we applied for points belonging to a certain height interval and time interval. The colors indicate the results of the DBSCAN clustering step, in which we have used the parameter values  $\epsilon = 0.075$  m and  $\text{minPts} = 12$ . (b) The same points after performing robust, RANSAC-based circle fitting using 3 cm as the inlier threshold and 0.7 as the lowest acceptable inlier ratio. Note that there are still a few noise points present close to the edges of the clusters 1 and 2.



**Fig. 6.** (a) Simulated data points belonging to the first cluster of the data set originally shown in Fig. 5. The dashed black line shows the circular fit obtained with the hyper-accurate circle fit algorithm, whereas the black arrow depicts the center of mass of the data points as compared with the center of the fitted circle (red cross). (b) The same points as in panel (a) but rotated such that the vector connecting the circle center and the center of mass is aligned with the x axis. In order to find the noise points close to the edges of the arc, we first sort the points based on the angle that they make with respect to the x direction. Subsequently, we go through the points in the sorted order and compute all the central angles between consecutive points. As illustrated in the figure, a central angle exceeding a threshold value  $\Delta\theta_{\max} = 10^\circ$  indicates the beginning of a new sub arc. (c) The result of applying arc division algorithm. Different colors correspond to different sub arcs. (d) Arcs obtained from the data set originally shown in Fig. 5 after applying the arc division algorithm iteratively. Note that the algorithm manages to filter out practically all of the noise points close to the edges of the arcs.

measurement errors, and they can have a large impact on the circle fitting if they are not removed (Forsman et al., 2016; Forsman et al., 2018). Therefore, we tried to filter out such noise points by applying the following arc division algorithm for each of the clusters separately:

1. We fitted a circle to the data points within a single cluster using the hyper-accurate circle fit (Al-Sharadqah and Chernov, 2009) in order to find the center  $(x_0, y_0)$  of the circular fit as illustrated in Fig. 6(a).
2. Subsequently, we calculated the angles between neighboring points as compared with the circle center. The neighboring points with angles larger than  $\Delta\theta_{\max} = 10^\circ$  were signed into different sub-clusters (=sub-arcs). This process is illustrated in Figs. 6(b-c).

Note that it is useful to rotate the points such that the center of mass vector of the cluster aligns with the x axis due to the discontinuity of the atan2 function. To refine the clustering even further, we applied the arc division algorithm iteratively for 5 times.

In order to determine which clusters correspond to tree trunks, we checked the features of the clusters against the following heuristically chosen quality criteria after fitting a circle to the data points using the hyper-accurate fit. We accepted a cluster if.

1. It contained at least  $N_{\min} = 50$  points.
2. The standard deviation of the radial residuals was below  $\sigma_R = 1.5$  cm.
3. The radius of the fitted circle was larger than  $R_{\min} = 4$  cm but smaller than  $R_{\max} = 40$  cm.
4. The central angle corresponding to the arc exceeded  $\theta_{\min} = 0.6\pi$  rad =  $108^\circ$ . Note that the central angle of the arc candidate can be conveniently estimated after rotating the center of mass of the data points to align with the x axis as in the arc division algorithm.

Having extracted arcs for all the time and height intervals, we clustered the extracted arc centers using the DBSCAN algorithm in the xy plane in order to group the arcs into trees. In our implementation, we used the parameter values  $\text{minPts}_2 = 5$  and  $\varepsilon_2 = 25$  cm. This implies that a particular tree was detected only if our arc extraction algorithm found at least 5 good quality arcs corresponding to the tree. Note that our arc extraction algorithm typically found 100–1000 arcs for a single tree indicating that the threshold  $\text{minPts}_2$  was chosen low enough. Note also that the neighborhood radius  $\varepsilon_2$  was chosen to equal the typical DBH of trees since the typical DBH sets an approximate lower bound for the inter-tree distance. Additionally, we required that the arcs of a single

tree had to range at least 1 m in the z direction.

After the extraction and clustering of the arcs, we utilized the workflow proposed by Hyypä et al. (2020) in order to obtain high-quality stem curve estimates despite of the positional drift of the scanner that is affecting the SLAM-corrected point cloud. In the rest of this section, we provide a summary of this workflow but a more detailed description of the methods together with schematic figures can be found in Hyypä et al. (2020). First, we estimated the growth direction of individual trees using the principal component analysis (PCA). Subsequently, we applied the arc matching algorithm. The goal of the matching algorithm was to determine the stem diameter at the mid-points of the height intervals ( $z_j = 1.2\text{m} + j \times 0.4\text{ m}$ ,  $j = \{0, 1, 2, \dots\}$ ) by optimally matching the extracted arcs within each height interval. In the matching, only such height intervals containing at least 2 arcs were taken into account in order to increase the robustness and reliability of stem curve extraction. In brief, the arc matching algorithm iterates through the following process:

1. On the first iteration, we fitted a circle to each of the arcs separately using the hyper-accurate fit. Then, we shifted each arc such that the center of the circular fit coincided with the origin after the shift.
2. We fitted a single circle to all of the arcs together such that the center of the fitted circle was fixed to the origin. This fit resulted in a radius estimate  $R$ .
3. Next, we fitted a separate circle to each of the arcs such that the radii of the fitted circles were all fixed to  $R$ . Again, all the arcs were shifted such that the centers of the fitted circles coincided with the origin after the shifts. The instructions 2 and 3 were iterated for 5 times in order to match the arcs optimally.

Note that we performed the circle fitting in the plane perpendicular to the average growth direction of the tree that we had previously obtained using the principal component analysis. This inclination angle correction improves the modeling accuracy for trees with inclined stems since it effectively makes the circle fitting equivalent to cylinder fitting.

To robustify the stem curve extraction process even further, we used a simple outlier detection scheme. The diameter estimate  $D_j$  obtained by applying the arc matching algorithm at the height of  $z_j$  was classified as outlying using the following criteria.

1. First, we searched for the  $k$  nearest height intervals for the height  $z_j$  (including the height interval itself), and computed the median (MEDIAN) and median absolute deviation (MAD) based on the diameter estimates of these  $k$  height intervals. If the tree had more than 5 diameter estimates at different heights associated with it, we used  $k = 5$ . Otherwise, we set  $k$  to equal the number of diameter estimates corresponding to the tree. The diameter estimate  $D_j$  was regarded as an outlier if
  - (a)  $|D_j - \text{MEDIAN}| > 2 \times \text{MAD}$ , and
  - (b)  $|D_j - \text{MEDIAN}| > 3.0\text{ cm}$ .

After removing the clearly outlying diameter estimates, we obtained the final stem curve estimate by fitting a smoothing cubic spline (see, e.g., De Boor et al., 1978; Pollock et al., 1993) to the diameter estimates at different heights. When fitting the smoothing spline, each diameter estimate was weighted with the corresponding uncertainty estimate. Thus, diameter estimates with high uncertainty had a lower impact on the fit as diameter estimates with low uncertainty. Note also that we chose the optimal value of the smoothing parameter using leave-1-out cross validation.

The DBH was primarily obtained by evaluating the fitted smoothing spline at the height of  $z = 1.3\text{ m}$ . However, if the lowest extracted diameter estimate was located above  $z = 1.3\text{ m}$ , the smoothing spline could not be used to estimate the DBH. If the stem curve had been extracted from a sufficiently wide height range ( $> 3\text{ m}$ ), the DBH was

obtained by fitting a linear model to the lowest 3 meters of the smoothing spline and subsequently, evaluating the linear model at the height of  $z = 1.3\text{ m}$ . If the stem curve was extracted only from a narrow height range ( $< 3\text{ m}$ ), we fitted a square root function (see Eq. (2)) to the stem curve, and then extrapolated the DBH by estimating the fit at the breast height.

### 3.3. Non-stem-based tree detection algorithm

In this section, we propose a tree detection algorithm based on robust vertical line fitting that is capable of detecting both trees with visible and occluded stems. The algorithm has been designed for trees with close-to-vertical stems in relatively sparse forests. Additionally, the proposed algorithm is suitable for point clouds collected with any technology that ensures that the positional drift of the scanner is approximately smaller than the average diameter of the trees. We used the proposed workflow (1) to show that almost all of the trees on the test sites can be detected even though their stems are occluded and (2) to find accurate tree locations from the above-canopy UAV data, which enables registering the under-canopy and above-canopy point clouds that are in different coordinate frames. The working principle of the tree detection algorithm is illustrated in the schematic in Fig. 7.

As a first step in the proposed tree detection algorithm, we constructed a simplified voxel-based representation of the point cloud. The point cloud was divided into voxels having a lateral width of  $L_{xy} = 25\text{ cm}$  in the x and y directions and a vertical width of  $L_z = 40\text{ cm}$  in the z direction. Voxels containing at least  $N_{\text{voxel}} = 50$  points were marked as full in order to filter out points located in regions with a low point density. To identify regions that potentially correspond to trees, we applied the 2D DBSCAN clustering algorithm for the full voxels at all the different heights intervals (with a width of 40 cm) ranging from the height of  $z = 1.5\text{ m}$  to  $z = 10.0\text{ m}$ . In the DBSCAN clustering, the minimum point number threshold was chosen as 1 and the cluster radius was set to  $\epsilon_3 = 50\text{ cm}$ . For each of the clusters, an effective circular representation was constructed by assigning the circle center to the center of mass of the cluster and choosing the effective cluster radius based on the area of the cluster as

$$r_{\text{eff}} = \sqrt{\frac{A}{\pi}}, \quad (5)$$

where  $A$  represents the area of the cluster based on the number of voxels belonging to the cluster.

Subsequently, a rectangular cell grid with a cell width of 10.0 m was set up in the xy plane and the clusters were assigned to these cells based on their locations. We applied a RANSAC-inspired vertical line fitting procedure for the clusters located within each cell. The vertical line fitting process can be summarized as follows.

1. Loop through the clusters within the given cell and fit a vertical line through the current cluster center. Find the number of inliers by counting the number of clusters that are located closer to the vertical line than their effective cluster radii  $r_{\text{eff}}$ . Keep track of the vertical line with the most inliers.
2. Accept the best vertical line if it is associated with at least 5 inlying clusters. Delete these inlying clusters from the list of available clusters and repeat the process until the best vertical line goes through less than 5 clusters.

Having performed the vertical line fitting in all the cells, we looped through the fitted vertical lines and searched for all the clusters that were located closer than  $1.5r_{\text{eff}}$  from a given vertical line. This step was required since each cluster was used at most once in the vertical line fitting process described above. Due to reassigning clusters to the vertical lines, a single clusters could be assigned to multiple vertical lines. Consequently, clusters corresponding to multiple vertical lines were

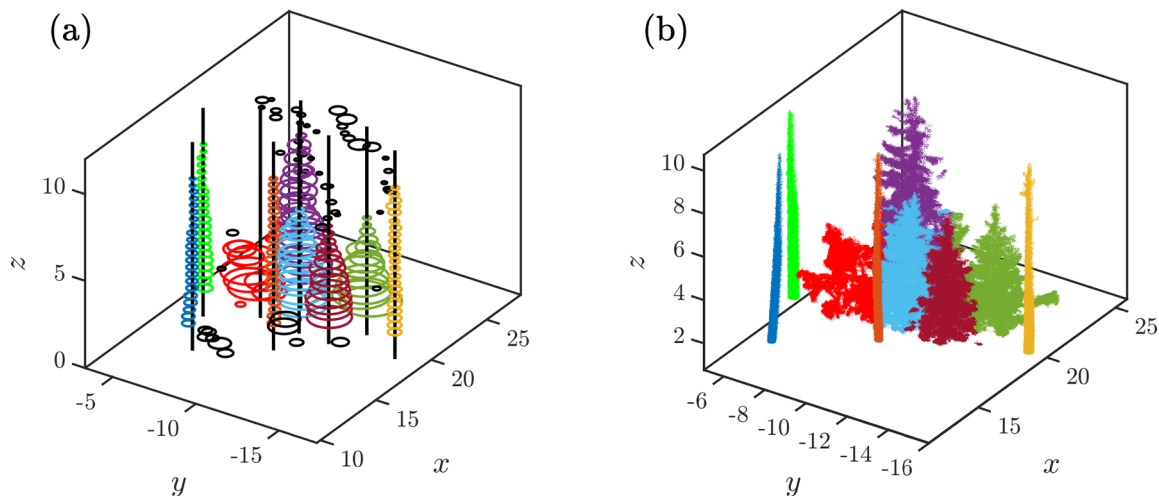


**Fig. 7.** (a) Schematic of the tree detection algorithm based on a small region located in the obstructed plot. The figure shows the effective circles representing the clusters obtained by applying DBSCAN clustering for the voxel-based representation of the point cloud. The results of the vertical line fitting are represented with solid black lines. Clusters corresponding to the same vertical line, i.e., tree are colored with the same color, whereas black circles represent clusters that do not belong to any tree. Note that in the figure, we have already refined the clustering by splitting clusters that belonged to multiple trees. (b) Segmentation of the point cloud based on the tree detection algorithm.

split such that each voxel was assigned to the closest vertical line based on the weighted distance metric  $\|\cdot\|_2/r_{\text{eff}}$ , where  $\|\cdot\|_2$  refers to the ordinary Euclidean norm. After, splitting the clusters, each cluster belonged to at most one vertical line. By using the newly assigned clusters, the location of each vertical line was re-fitted by giving more weight to smaller clusters

$$x = \frac{\sum_i x_i r_{\text{eff},i}^{-2}}{\sum_i r_{\text{eff},i}^{-2}}, \quad (6)$$

$$y = \frac{\sum_i y_i r_{\text{eff},i}^{-2}}{\sum_i r_{\text{eff},i}^{-2}}, \quad (7)$$

where  $(x_i, y_i)$  refers to the center of the  $i$ th cluster associated with the given vertical line and  $r_{\text{eff},i}$  is the corresponding effective radius. Finally, a vertical line was classified as a tree if it contained at least 10 clusters. In Fig. 7(b), we illustrate the tree detection and segmentation results for a single cell in the obstructed plot. Note that the algorithm can even detect spruces with partly overlapping branches provided that suitably chosen parameter values are used.

### 3.4. Stem volume estimation using a combination of under-canopy and above-canopy UAV laser scanning data

In order to estimate the stem volumes for the trees with detected stems, we derived the tree height from the point clouds obtained with the above-canopy flying UAV. To this end, we first generated the DTM for the above-canopy point clouds and subtracted the ground level from the  $z$  coordinates of all the points. Importantly, the coordinate frames of the point clouds collected with the under-canopy and above-canopy UAVs were different since the point clouds obtained with the above-canopy flying UAV were georeferenced, whereas the under-canopy point clouds were not. To find the two-dimensional Euclidean transformation between the point clouds, we first used the tree detection algorithm described in the previous section to detect the locations of all trees in the above-canopy point cloud. Since the number of stem points was much lower in the above-canopy point cloud as compared with the under-canopy point cloud, we used the parameter values  $L_z = 50$  cm and  $N_{\text{voxel}} = 1$  in the tree detection algorithm. The rest of the parameters were kept at their default values. Subsequently, the stem locations extracted from the under-canopy UAV laser scanning data were compared against the tree locations found from the above-canopy

point cloud in order to find the rotation angle and translation between the point clouds.

Having matched the point clouds, we determined the tree height for each tree whose stem had been previously found from the under-canopy UAV laser scanning data. For a given tree, we first found all the points in the above-canopy UAV point cloud that were located within 1 m from the 3D line defined by the growth direction of the tree. Subsequently, we divided the  $z$  axis into height intervals of width 1.0 m and counted the number of points within the height intervals. For big trees having a diameter larger than 20 cm, the tree top was identified as the highest height interval containing at least 10 points and the tree height was obtained as the average  $z$  coordinate of the 5 highest lying points in the given height interval. For small trees having a diameter smaller than 20 cm, the tree top was assumed to be located in the lowest height interval that was above the highest extracted good-quality arc and contained less than 10 points. In this case, the tree height was acquired by computing the average of 5 highest lying points in the height interval below the interval corresponding to the tree top. Note that the division to small and large trees was made to accurately extract the heights of suppressed trees shadowed by taller trees.

After extracting the stem curve from the under-canopy UAV laser scanning data and the tree height from the corresponding above-canopy UAV data, we estimated the stem volume using the same method as for the reference stem volumes described in Section 2.4. Briefly, we fitted the parabolic and square root functions given by Eqs. (1) and (2) to the stem curve radii appended with the tree height. Subsequently, the stem volume was obtained by integrating the fits as described in Eq. (3).

### 3.5. Statistical analysis

In this section, we briefly review the statistical tools used for assessing the performance of the under-canopy UAV laser scanning. We quantify the accuracy of stem detection using the concepts of completeness and correctness

$$\text{Completeness} = \frac{\text{Number of reference trees found}}{\text{Total number of reference trees}} \times 100\%, \quad (8)$$

$$\text{Correctness} = \frac{\text{Number of reference trees found}}{\text{Total number of trees found}} \times 100\%, \quad (9)$$

where the total number of trees found refers to all the trees found by the algorithm within the test site.

As usual, the bias and root-mean-square error (RMSE) of a variable  $x$  (e.g., DBH, tree height) are evaluated using the following equations

$$\text{bias} = \sum_{i=1}^N \frac{x_i - x_{i,\text{ref}}}{N}, \quad (10)$$

$$\text{RMSE} = \left( \sum_{i=1}^N \frac{(x_i - x_{i,\text{ref}})^2}{N} \right)^{1/2}, \quad (11)$$

where  $N$  is the number of successfully found trees,  $x_i$  refer to the estimates obtained with the algorithm, and  $x_{i,\text{ref}}$  denote the corresponding reference values. The corresponding relative bias and RMSE are defined as follows

$$\text{bias} - \% = \frac{\text{bias}}{\bar{x}_{\text{ref}}} \times 100\%, \quad (12)$$

$$\text{RMSE} - \% = \frac{\text{RMSE}}{\bar{x}_{\text{ref}}} \times 100\%, \quad (13)$$

where  $\bar{x}_{\text{ref}}$  denotes the average value based on the reference measurements

Note that the bias and RMSE have to be computed in a slightly different way for the stem curve estimates since the number of diameter estimates varies from tree to tree. We define the bias and RMSE of a single stem curve as

$$\text{bias}_i = \sum_{j=1}^{N_i} \frac{D_i(z_j) - D_{i,\text{ref}}(z_j)}{N_i}, \quad (14)$$

$$\text{RMSE}_i = \left( \sum_{j=1}^{N_i} \frac{(D_i(z_j) - D_{i,\text{ref}}(z_j))^2}{N_i} \right)^{1/2}, \quad (15)$$

where  $\text{bias}_i$  and  $\text{RMSE}_i$  are the bias and RMSE corresponding to the stem curve of the  $i$ th tree,  $D_i(z_j)$  is the extracted diameter at height  $z_j$  based on the smoothing spline fit, and  $D_{i,\text{ref}}(z_j)$  is the corresponding reference diameter. Note that the extracted diameter is compared with those reference diameters that are located within the height interval of the extracted stem curve. Thus, the number  $N_i$  varies from tree to tree.

The total bias and RMSE of the stem curve estimation can then be computed as

$$\text{bias}_{\text{tot}} = \sum_{i=1}^N \frac{\text{bias}_i}{N}, \quad (16)$$

$$\text{RMSE}_{\text{tot}} = \left( \sum_{i=1}^N \frac{\text{RMSE}_i^2}{N} \right)^{1/2}, \quad (17)$$

where the summation runs over the matched trees.

## 4. Results

### 4.1. Stem and tree detection using under-canopy UAV laser scanning data

Before comparing the tree attributes of the extracted and reference stems, we matched the extracted stems with the corresponding reference trees by finding the optimal rotation and translation between the local coordinate system of the under-canopy UAV point cloud and the global coordinate system. After applying this Euclidean transformation, we matched each detected stem with the closest reference tree provided that the distance between the trees was less than 0.5 m.

In the sparse plot, our stem detection algorithm described in Section 3.2 managed to detect correctly 39 out of the 42 reference trees, i.e., the completeness of stem detection was 93%. As illustrated in Fig. 8(a), the algorithm could detect all of the 39 pines but none of the 3 spruces due to the poor stem visibility. Additionally, there were no falsely detected stems within the test site indicating that the correctness of stem detection was 100%.

In the obstructed site, our stem detection algorithm detected correctly all of the 30 pines and 4 out of 5 birches but only 2 of the 8 spruces. Therefore, the completeness of stem detection was 84% when all of the trees were considered. As can be seen from Fig. 8(b), there were again no falsely detected stems within the test site indicating that the correctness of stem detection was 100%.

Using the tree detection algorithm presented in Section 3.3, we were able to detect 41 out of the 42 trees in the sparse plot corresponding to a completeness level of 98%. The algorithm interpreted two spruces with highly overlapping branches as a single tree resulting in the omission of a single spruce. In the obstructed plot, the tree detection algorithm detected 40 out of the 43 trees. The algorithm interpreted 4 small spruces with highly overlapping branches as a single spruce resulting in the omission of three spruces. In both of the test sites, the correctness of tree detection was 100%. Note that the detected location of one birch is off by approximately 1 m as compared with its reference location in Fig. 8(b) due to its highly inclined stem.

### 4.2. DBH estimation using under-canopy UAV laser scanning data

Using the definitions in Section 3.5, the bias of the DBH estimates was found to be 0.31 cm (1.1%) in the sparse plot, and 0.29 cm (1.0%) in the obstructed plot. As illustrated in Fig. 9(a), the corresponding RMSE values for the DBH were 0.69 cm (2.2%) in the sparse plot, and 0.92 cm (3.1%) in the obstructed plot. Fig. 9(b) illustrates the high accuracy of the DBH estimation by showing a scatter plot of the estimated DBH values against the reference measurements. The coefficient of determination was 0.98 for the sparse plot and 0.99 for the obstructed plot. Note that the sparse test site contained a single tree, for which the DBH had to be extrapolated since the lowest extracted diameter estimate was located above  $z = 1.3$  m. The obstructed plot contained two such trees.

### 4.3. Stem curve estimation using under-canopy UAV laser scanning data

In Fig. 10(a), we illustrate the performance of the stem curve extraction algorithm by showing a scatter plot of the estimated stem diameters and the corresponding reference measurements. Based on the scatter plot, we note that the coefficient of determination  $R^2$  was 0.91 for the sparse plot and 0.96 for the obstructed plot. In Fig. 10(b), we show a distribution of the heights, up to which the stem curve was successfully determined. Note that the height interval, where the stem curve can be reliably extracted, is tree specific and depends mostly on the visibility of the stem. On average, our method was able to extract the stem curve up to the height of 7.5 m in the sparse plot, and up to the height of 6.6 m in the obstructed plot.

Using the definitions presented in Section 3.5, the total bias of the stem curves was found to be 0.42 cm (1.8%) in the sparse plot and 0.55 cm (2.0%) in the obstructed plot as illustrated in Fig. 10. The corresponding RMSE values were 1.2 cm (5.0%) in the sparse plot and 1.4 cm (5.2%) in the obstructed plot. In Fig. 10(c), we show the relative RMSE and bias of the stem curve estimates as a function of height. Based on the figure, we can observe that the RMSE is the smallest in the height interval 1.0–1.5 m, and the RMSE increases with increasing height. Below the height of  $z = 5$  m, the relative RMSE is below 5.0% for both the plots, whereas it has a value in the range of 5–10% at the heights of 5.0–9.0 m. Interestingly, also the bias of the stem curve estimates increases with increasing height from approximately 0% at the height of 3.0 m to nearly 8% at the height of 8.0 m. In Figs. 11–13, we show a few examples of the stem curves extracted with our method for each of the three tree species present in the test sites.

### 4.4. Stem volume estimation using a combination of under- and above-canopy UAV laser scanning data

In this section, we consider the accuracy of the stem volume estimation based on a combination of under- and above-canopy UAV laser

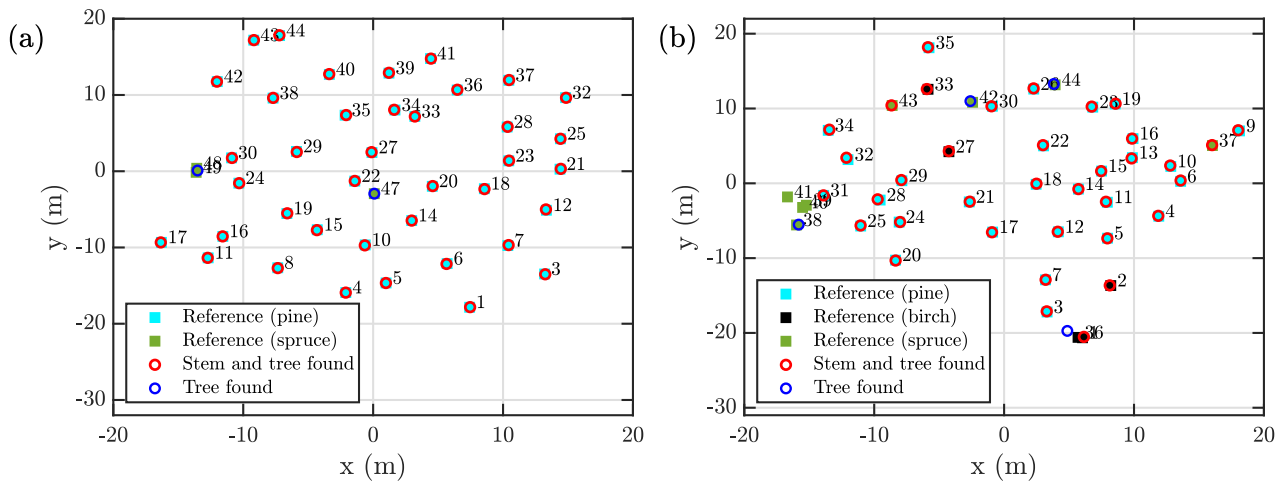


**Fig. 8.** Detected trees (circles) and the reference trees (filled squares) (a) in the sparse and (b) in the obstructed plots. The tree species are indicated with colors: pines are denoted with light blue, birches with black and spruces with dark green. We use red circles to denote the locations of trees whose stem was successfully detected using the arc-based algorithm. Blue circles denote trees whose stem could not be detected but whose location could still be found using the separate tree detection algorithm described in Section 3.3.

scanning data using the process described in Section 3.4. Using the point cloud collected with the above-canopy flying UAV, we extracted the tree heights for trees with a detected stem with a bias of 0.34 m (1.5%) in the sparse plot and with a bias of -0.14 m (-0.6%) in the obstructed plot. The corresponding RMSE values were 0.53 m (2.4%) for the sparse plot and 0.77 m (3.1%) for the obstructed plot.

By employing the stem curves extracted from under-canopy UAV laser scanning data and tree heights obtained from above-canopy UAV laser scanning data, we were able to derive the stem volumes of individual trees with a bias of 0.023 m<sup>3</sup> (3.8%) in the sparse plot, and with a bias of 0.031 m<sup>3</sup> (3.7%) in the obstructed plot. The corresponding RMSE values were 0.063 m<sup>3</sup> (10.1%) in the sparse plot, and 0.087 m<sup>3</sup> (10.1%) in the obstructed plot. In Fig. 10(d), we illustrate the high precision of the stem volume estimation by showing a scatter plot of the stem volume estimates and the corresponding reference values. The coefficient of determination R<sup>2</sup> was found to be 0.90 for the sparse plot and 0.99 for the obstructed plot.

4.5. Species-wise results

In this section, we additionally present the species-wise results for stem detection, DBH estimation, stem curve extraction and stem

volume estimation since the characteristic properties of trees vary greatly between the different species. In Table 2, we present the results for stem and tree detection averaged among different tree species. As already noted in Section 4.1, the stem and tree detection results are close to 100% for pines and birches, whereas the detection rate for spruces is markedly worse. The low stem detection rate for the spruces is due to the severe occlusion of their stem as can be seen from Fig. 14, which shows a photograph and a point cloud of a spruce whose stem could not be detected. The tree detection rate for spruces is 64%, i.e., much higher than the stem detection rate but still far from 100%. This is due to the fact that the spruces on the test sites tend to grow close to each other, on account of which their branches overlap at several heights as can be seen from the point cloud depicted in Fig. 7(b). Hence, our tree detection algorithm might interpret multiple spruces as a single tree. This problem can potentially be alleviated by using optimized parameter values instead of heuristically chosen ones in the tree detection algorithm described in Section 3.3, but this would most probably make the algorithm more prone to false detection of trees.

In Table 3, we present the species-wise results for DBH, stem curve and stem volume estimation for those trees whose stem was detected. Based on the table, we can note that the results are the best for pines that are characterized by a straight, circular stem with only slight

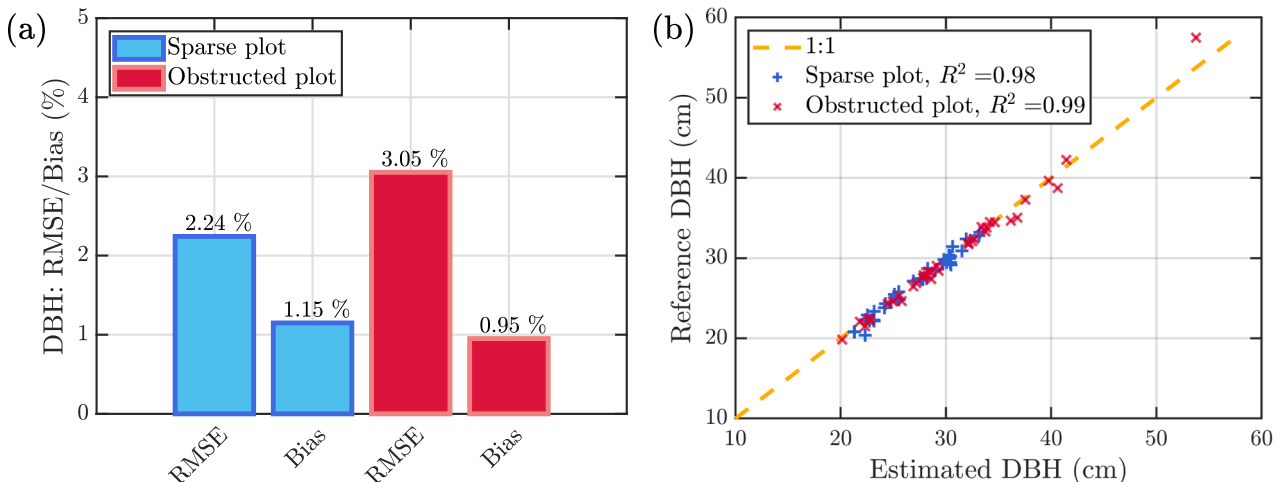


**Fig. 9.** (a) Relative root-mean-squared error (RMSE) and bias of the DBH estimates on an individual tree level in the sparse plot (light blue) and in the obstructed plot (dark red). (b) Scatter plot of the estimated DBH values vs the reference values for the sparse plot (blue pluses) and the obstructed plot (red crosses).

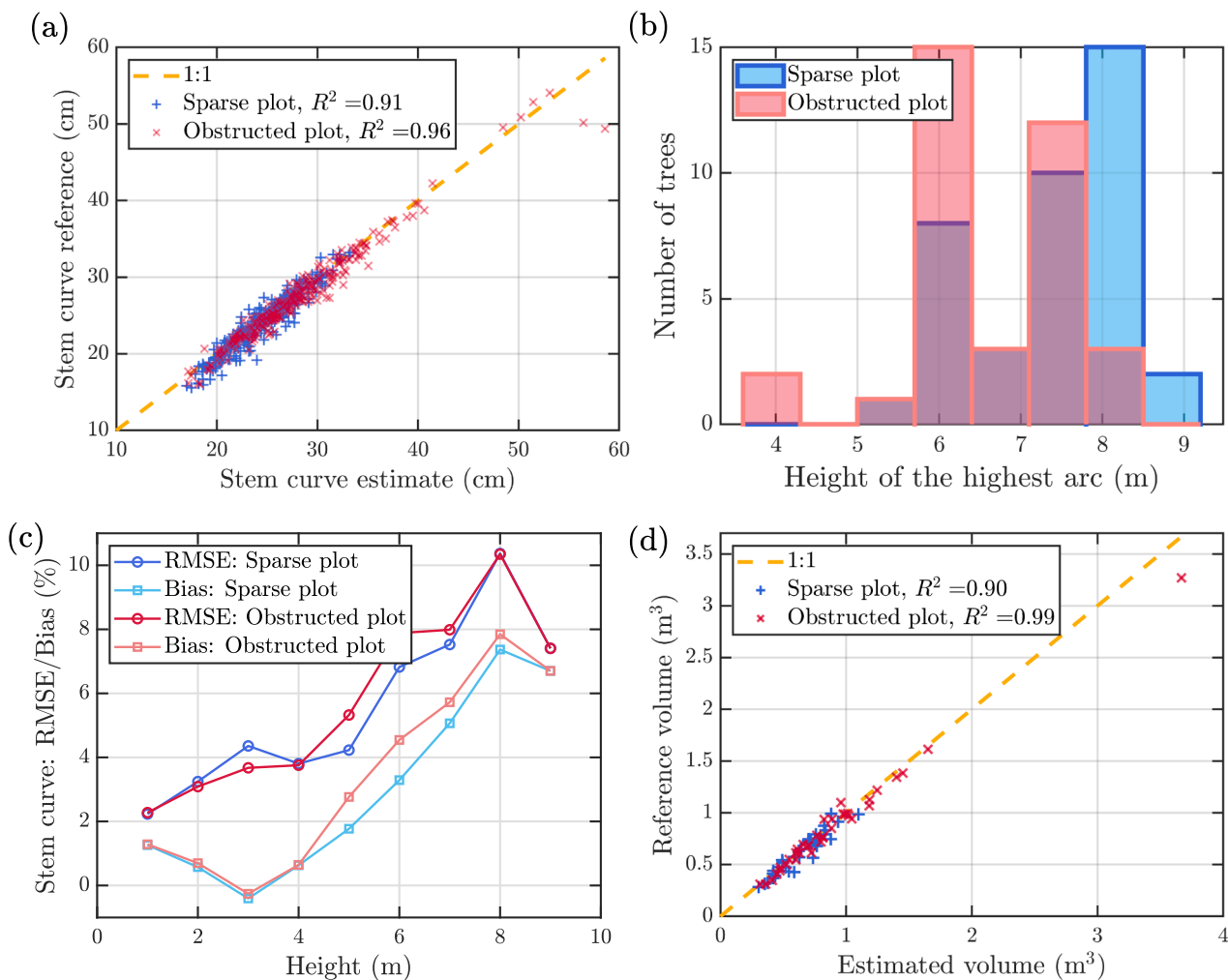


**Fig. 10.** (a) Scatter plot of the stem diameters estimated with under-canopy UAV laser scanning vs the corresponding results from reference measurements for the sparse plot (blue pluses) and the obstructed plot (red crosses). Note that the figure includes the diameter estimates at all different heights. (b) Distribution of the heights, up to which the stem curve was successfully determined in the sparse and obstructed plot. (c) The relative RMSE and bias for stem diameters estimated with under-canopy UAV laser scanning as a function of the height for both the sparse (blue) and obstructed plot (red). (d) Scatter plot of the stem volumes estimated using the combination of under-canopy and above-canopy UAV laser scanning vs the corresponding reference volumes for the sparse plot (blue pluses) and the obstructed plot (red crosses).

occlusion from branches. Importantly, the RMSE of stem curve estimation is also significantly below 10.0% for the detected birches and spruces, and the RMSE of stem volume estimation is below 15% for these trees despite of the severe occlusion that some of the detected trees suffered from. However, it pays to bear in mind that the number of birches and spruces on the test sites is fairly small, and therefore one should not draw too far-reaching conclusions based on these results.

To further illustrate the performance of our algorithm for different tree species, we show photographs, raw point clouds, matched point clouds and the extracted stem curve for one tree of each species in Figs. 11–13. As can be seen from Fig. 11, our algorithm can extract the stem curve for pines approximately up to the height of 8 m with a good precision. Note also that the positional drift of the scanner can cause distortion of the stems in the raw point cloud as illustrated in Fig. 11(c). Importantly, the arc matching algorithm can eliminate this distortion as shown in 11(d), thus greatly improving the accuracy of stem curve estimation.

In Fig. 12, we illustrate the stem curve estimation for a large birch in the obstructed plot. Note that the birch represents one of the most difficult birches to model on the obstructed test site due to its fairly non-circular stem and its relatively high number of branches above the height of  $z = 5.0$  m. Nevertheless, our stem curve estimation algorithm

can predict the stem curve of the birch with a reasonable accuracy, especially, at low heights.

Finally, Fig. 13 illustrates a spruce whose stem was detected from a narrow height interval despite of the severe occlusion of the stem. Figs. 13(c-d) illustrate the robustness of the arc extraction algorithm by showing that the algorithm is also capable of detecting stem points for very difficult trees.

## 5. Discussion

### 5.1. Comparison to past studies

The stem and tree detection rates obtained in this study are at the level of typical detection rates obtained in MLS studies. Using hand-held mobile laser scanners, the previously reported stem detection rates have varied between 80 to 95 percent in relatively sparse structured forests (Cabo et al., 2018; Bauwens et al., 2016; Marselis et al., 2016; Del Perugia et al., 2019). Liang et al. (2014a) obtained 87.5% for the tree mapping accuracy in boreal forest conditions by utilizing a laser scanner mounted on an all-terrain vehicle. Using a mobile backpack laser scanner, Hyypä et al. (2020) detected 84–95% of the stems on the same 32 m × 32 m test sites that were used in this study.

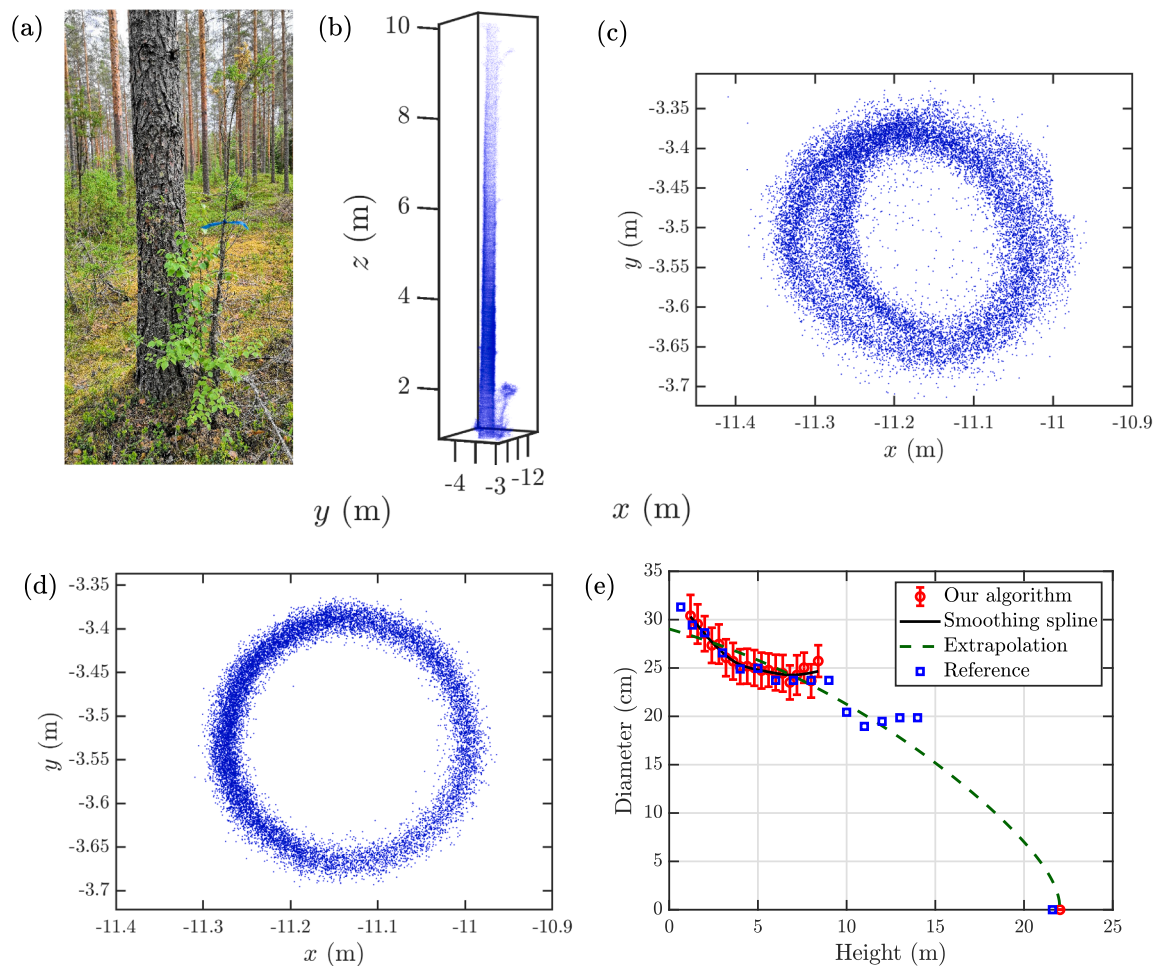


**Fig. 11.** (a) Photograph of a pine located in the sparse plot. (b) The raw point cloud of the pine obtained with under-canopy UAV laser scanning. (c) Cross section of the point cloud corresponding to the pine in the height interval  $z \in [2.0\text{m}, 2.5\text{m}]$ . Note the distortion in the point cloud due to the positional drift of the SLAM algorithm. (d) The same cross section as in panel (c) after performing the arc extraction and arc matching algorithms. Note that the remaining noise is due to the ranging accuracy of the scanner. (e) The stem curve (red circles) extracted for the pine shown in panel (a) using the arc-based method. Note that the stem curve is estimated using the under-canopy UAV laser scanning apart from the tree height that is obtained from above-canopy UAV laser scanning. The error bars of the stem curve correspond to the standard deviation of the circular fit. We also show the smoothing spline fit (solid black line) and the extrapolation of the stem diameter (dashed green line) used to compute the stem volume based on the effective fit obtained from Eqs. (1) and (2). The reference diameter measurements are shown with blue rectangles.

Based on our results, under-canopy UAV laser scanning can provide the DBH and stem curve of trees with a similar accuracy as multi-scan TLS measurements in boreal forest conditions. In previous multi-scan TLS studies conducted in boreal forest conditions, the DBH and stem curve have been obtained with an RMSE of 5–10% (e.g., Liang et al., 2018a; Liang et al., 2019). Recent studies using ground-based mobile laser scanning have resulted in the following accuracy for DBH estimation. Tomaštk et al. (2017) used Google Tango (Google LLC., California, USA), Cloud Compare (GPL) software with the Cloth Simulation Filter, and manual measurements of DBH in order to measure the DBH of trees with an RMSE of below 2 cm. Similar approaches by Hyypä et al. (2017) using automated circle fitting resulted in an RMSE of 0.73 cm, whereas Fan et al. (2018) obtained 1.26 cm for the error of DBH estimation. Using hand-held scanners, DBH has been obtained with an accuracy ranging from 1 to 4 cm in relatively sparse structured forests (Cabo et al., 2018; Bauwens et al., 2016; Marselis et al., 2016; Del Perugia et al., 2019). Recently, Hyypä et al. (2020) used backpack mobile laser scanning, a SLAM algorithm and the post-SLAM arc matching algorithm to derive the stem curve of trees with an RMSE of 5–6% in easy and medium-difficult boreal forests. Thus, our results for

DBH and stem curve estimation obtained with under-canopy UAV laser scanning have an RMSE on par with the past best studies based on MLS.

Furthermore, the combination of under- and above-canopy UAV laser scanning allowed us to derive the stem volume with an RMSE that is equivalent with the state-of-the-art multi-scan TLS methods that can reach an RMSE of approximately 10% in favourable forest conditions (see, e.g., Liang et al., 2014b). Interestingly, our results for stem volume estimation are even slightly better than the level of 15–20% obtained in comparable forest conditions by the international TLS benchmarking study (see Liang et al., 2018a). Earlier, only a few mobile laser scanning papers (Liang et al., 2019; Liang et al., 2018b; Bienert et al., 2018) have reported the accuracy of stem volume estimation. The presented errors (RMSE) for stem volume range from 20 to 50% even in relatively sparse boreal forest plots. Very recently, Hyypä et al. (2020) demonstrated that the stem volume could be obtained with an RMSE of approximately 10% in easy and medium-difficult boreal forest conditions by using a backpack mobile laser scanning and a carefully designed point cloud processing workflow, which takes into account the positional drift of the scanner that remains even after the SLAM correction.

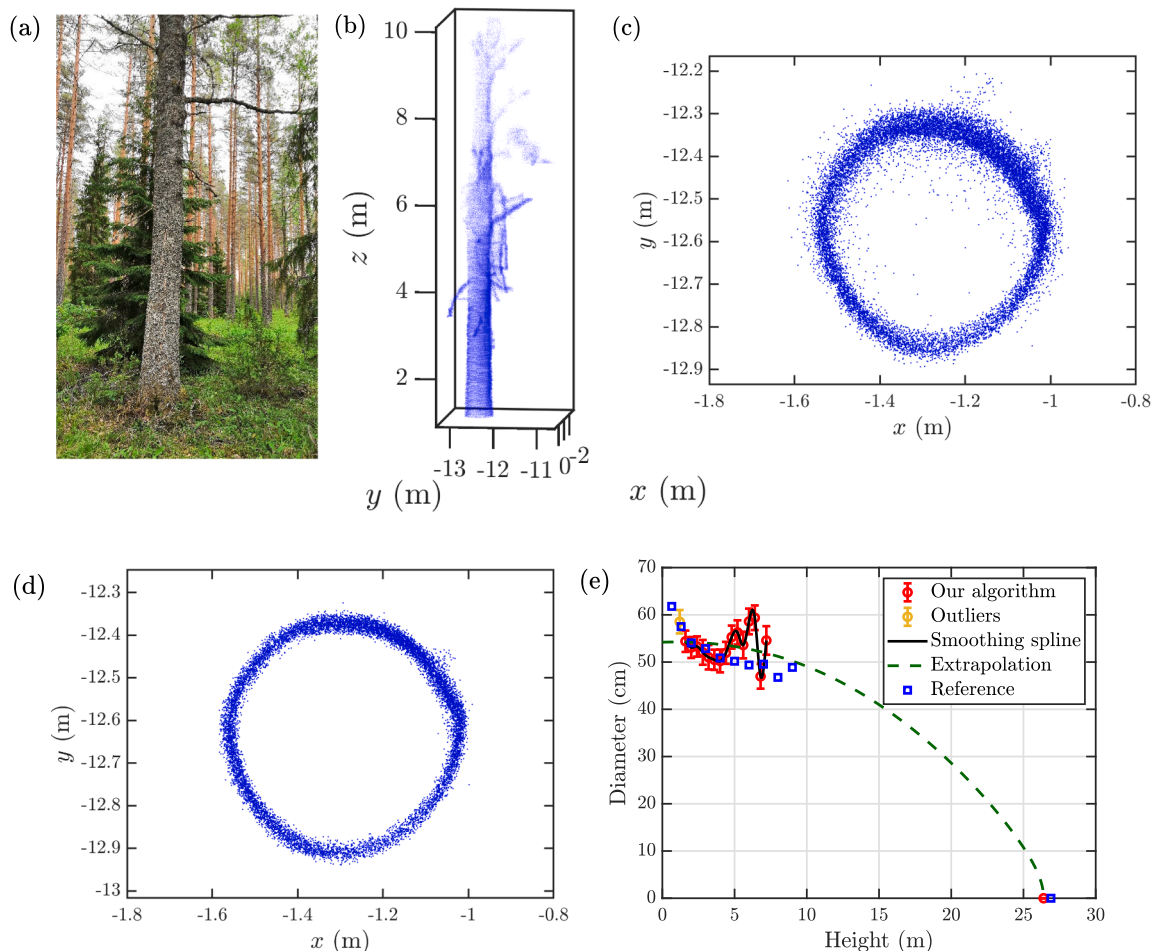


**Fig. 12.** (a) Photograph of a large birch located in the obstructed plot. (b) The raw point cloud of the birch obtained with under-canopy UAV laser scanning. (c) Cross section of the point cloud corresponding to the birch in the height interval  $z \in [2.0\text{m}, 2.5\text{m}]$ . (d) The same cross section as in panel (c) after performing the arc extraction and arc matching algorithms. (e) The stem curve (red circles) extracted from the birch shown in panel (a) using the arc-based method. Note that the stem curve is estimated using the under-canopy UAV laser scanning apart from the tree height that is obtained from above-canopy UAV laser scanning. The error bars of the stem curve correspond to the standard deviation of the circular fit. We also show the smoothing spline fit (solid black line) and the extrapolation of the stem diameter (dashed green line) used to compute the stem volume based on the effective fit obtained from Eqs. (1) and (2). The reference diameter measurements are shown with blue rectangles.

## 5.2. Feasibility considerations regarding under-canopy UAV laser scanning

Since the point clouds collected with the under-canopy flying UAV are more noisy than those obtained with TLS or the best MLS methods, we presume that the major reason for the high-quality results obtained in this study is the data processing workflow that takes into account the time-dependent positioning error of the scanner. Our data processing workflow included a correction of the positioning errors using both a real-time SLAM algorithm and a post-SLAM arc matching algorithm.

Another advantage of the under-canopy UAV measurements is that they are fast even when conducted manually as in this study. The time taken by the measurements can be reduced further if the fully-automatic concept described in Section 5.3 is implemented. We expect that several dozens of plots can be measured in one day by one surveyor with manual flying and up to 50 plots when utilizing the fully-automatic concept. In comparison, a two-person team can conduct conventional field measurements on two plots in one day if also the tree locations are to be measured. TLS measurements can be carried out for half a dozen of plots in one day by two surveyors when calibration objects are used to perform a multi-scan survey. Thus, the proposed concept is up to several tens times faster than the conventional measurements even when manual flying of the UAV is employed. This implies that under-canopy UAV laser scanning has great potential for

realizing accurate and fast forest field reference inventories in conditions, where the road network supports field data collection. Importantly, the fully-automatic concept illustrated in Fig. 16 can also be used for various other remote sensing and earth observation applications. However, there is a need to develop further the technologies related to all steps 1–6 in the robotic-assisted end-to-end approach before the fully-automatic concept can be realized in practice.

Furthermore, the algorithms proposed in this paper are feasible from the point of view of the computation time. Our Matlab implementation of the stem curve extraction algorithm can process a single point cloud containing approximately 50 million points in just under 20 min on a modern laptop computer. Furthermore, our Matlab implementation of the tree detection algorithm described in Section 3.3 runs in just under one minute for each of the point clouds. The two point clouds studied in this work cover an area of approximately  $70\text{ m} \times 70\text{ m} \approx 0.5\text{ ha}$  each. This implies that during a single day, our implementation of the algorithm could process a point cloud covering 36 ha assuming that the point density is on the order of  $1 \times 10^4\text{ pts/m}^2$ . With further parallelization and optimization, the running time of the proposed algorithm can possibly be reduced further.

As noted in Section 4.3, the RMSE of stem diameters was below 5% in the height interval  $z = 1\text{--}5\text{ m}$ , whereas the corresponding error in the height range  $z = 5\text{--}10\text{ m}$  was found to be between 5–10% and the

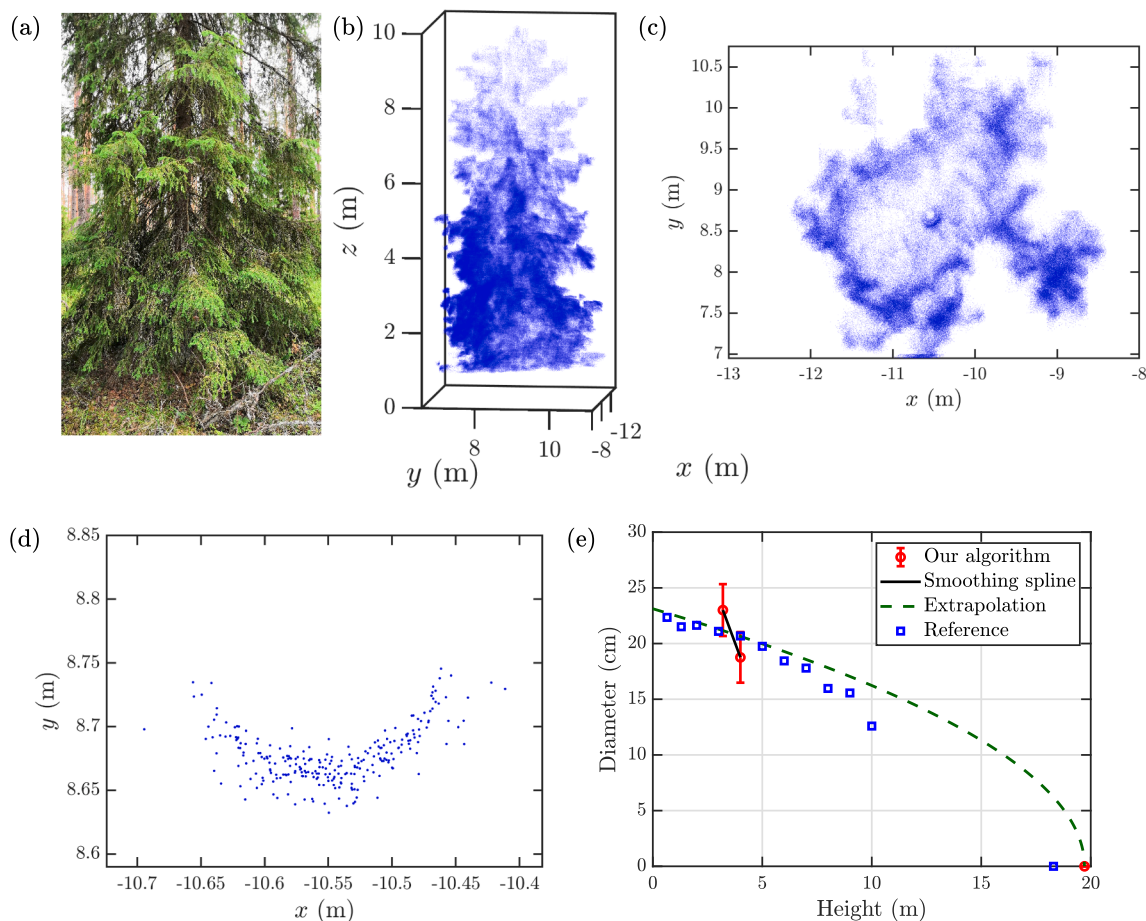


**Fig. 13.** (a) Photograph of a spruce located in the obstructed plot. (b) The raw point cloud of the spruce obtained with under-canopy UAV laser scanning. (c) Cross section of the point cloud corresponding to the spruce in the height interval  $z \in [2.5\text{m}, 3.5\text{m}]$ . (d) The same cross section as in panel (c) after performing the arc extraction and arc matching algorithms. Note that this is a close-up to the spruce stem as compared with panel (c). (e) The stem curve (red circles) extracted from the tree height that is obtained from above-canopy UAV laser scanning. The error bars of the stem curve correspond to the standard deviation of the circular fit. We also show the smoothing spline fit (solid black line) and the extrapolation of the stem diameter (dashed green line) used to compute the stem volume based on the effective fit obtained from Eqs. (1) and (2). The reference diameter measurements are shown with blue rectangles.

**Table 2**

Species-wise statistics of the stem and tree detection obtained by considering all the trees within the two plots.

Tree species	Number of trees	Stem detection		Tree detection	
		Completeness (%)	Correctness (%)	Completeness (%)	Correctness (%)
Pine	69	100%	100%	100%	100%
Birch	5	80%	100%	100%	100%
Spruce	11	18%	100%	64%	100%

diameters were systematically overestimated. There are a few reasons that could explain this observation. First, the growth of the stem diameters between the years 2014 and 2019 was calibrated by measuring the DBH in 2019 as explained above, and subsequently adding the change in the DBH to all the measured reference stem diameters. However, it is possible and even likely that the shape of a tree has changed during the 5 years. Therefore, the reference measurements are simply less accurate high above the ground for most of the trees. To support this finding, we show in Fig. 15 the stem curve of a pine whose stem diameter is clearly overestimated in the height interval  $z = 5\text{--}8\text{ m}$  as compared with the calibrated reference. In the figure, we also show the stem curve of the same tree extracted from mobile laser scanning data recorded in 2016 using a scan-line arc-based stem curve estimation method (Hyypä et al., 2020). By comparing the three stem curves of

the same tree, we can conclude with relatively high certainty that the stem diameter has grown much more in the height interval 5–8 m than at the breast height explaining the large RMSE. A recent paper (Luoma et al., 2019) studying the changes in stem tapering supports these findings: the largest decrease in tapering was detected especially with coniferous trees and was the largest with Scots pine trees. The trees tend to grow into the shape of a cylinder which change the tapering of the tree depending on the age of the tree.

Another potential reason for the height dependent RMSE is that the number of branches increases at heights high above the ground and simultaneously, the number of good quality arcs decreases. Both of these phenomena can reduce the accuracy of stem curve extraction at higher heights. In future studies, the reference data must be acquired with sufficient rigour to ensure that a reasonable quality assessment can

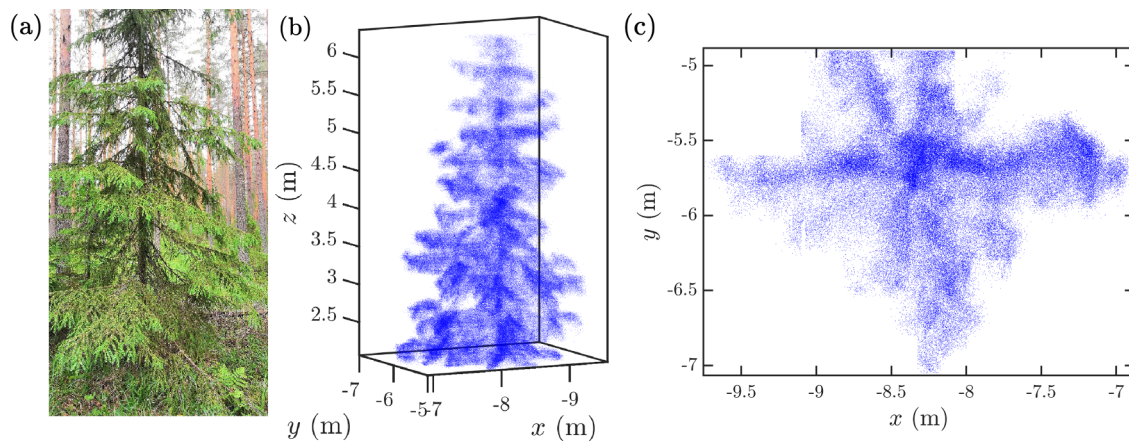


**Fig. 14.** (a) Photograph of a young spruce located in the obstructed plot. (b) The raw point cloud of the spruce obtained with under-canopy UAV laser scanning. (c) Cross section of the point cloud corresponding to the spruce in the height interval  $z \in [3.0\text{m}, 4.0\text{m}]$ . Note that the stem of the spruce is severely occluded and therefore, the stem could not be detected using the arc-based method. However, the spruce could still be detected by using the separate tree detection algorithm.

**Table 3**  
Species-wise statistics of the DBH, stem curve and stem volume estimation obtained by considering all the trees within the two plots.

Tree species	Detected stems	DBH		Stem curve		Stem volume	
		Bias-%	RMSE-%	Bias-%	RMSE-%	Bias-%	RMSE-%
Pine	69	1.3%	2.3%	2.0%	4.8%	3.2%	8.4%
Birch	4	-2.4%	5.0%	2.1%	7.4%	6.9%	14.6%
Spruce	2	2.4%	2.8%	-3.9%	6.4%	12.5%	13.2%

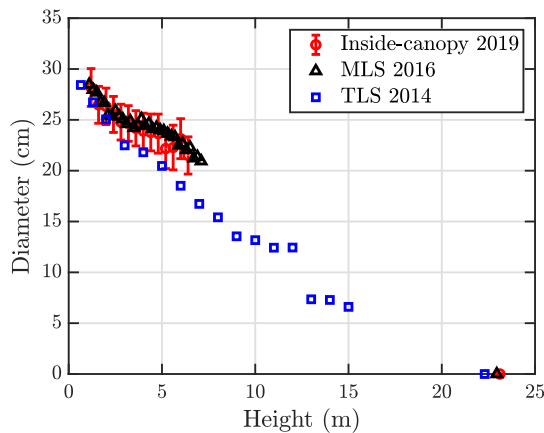


**Fig. 15.** Stem curve of an example tree based on three measurements conducted in different years: under-canopy flight in 2019 (red circles), mobile laser scanning in 2016 (black triangles) and terrestrial laser scanning in 2014 (blue squares).

be made.

Our stem curve extraction algorithm is suitable for the detection of trees with at least partly visible stems. Importantly, the algorithm can deal with a moderate amount of noise in the point cloud thanks to the RANSAC-based circle fitting step and the iterative arc division algorithm. Here, noise refers to the deviation of points from the surfaces of stems due to measurement errors, branches, or understory vegetation. A major cause of noise in the point cloud is due to reflections from branches, needles and leaves of the trees. Spruces are examples of such trees that are challenging to process with the approach presented herein due to the severe occlusion of the stem as illustrated in Figs. 13 and 14. As a result of the occlusion problem, the stems of especially young spruces might not be detectable even for the human eye in the point cloud as illustrated in Fig. 14.

Moreover, our approach requires further testing, particularly in dense, complex boreal forest conditions. It is, therefore, clear that different algorithmic approaches will need to be developed for different forest types; the algorithm presented by Liang et al. (2012) is an example of an approach that has the potential for working better within spruce canopies thanks to a PCA-based filtering step for stem point detection. However, this approach might not be directly applicable for the point clouds produced with the under-canopy flying UAV since the limited ranging accuracy ( $\pm 3$  cm) of the scanner gives rise to a fair amount of noise and the stems in the point cloud can be distorted due to the positional drift of the scanner. However, there are possibilities to improve the approach presented herein further by using intensity information, improved SLAM, improved sensors, the use of the outer shape of the tree to estimate trunk, and approaches more tolerant to noisy data. An interesting idea for future development would be to combine the point cloud collected using the under-canopy flying UAV with color information from a photogrammetric point cloud produced with structure from motion technology (Iglhaut et al., 2019). This could potentially enable efficient filtering of points reflected from leaves and needles that are characterized by green color.

### 5.3. Robotic-assisted surveying concept for the future

The robotic-assisted surveying concept envisioned for the future is illustrated in Fig. 16. First, an autonomous car is driven to a location adjacent to the forest plot to be surveyed. The UAV then flies from the autonomous car to the plot. The UAV with the laser scanners pointing downwards maps the forest plots first from above the canopy and obtains a georeferenced point cloud of the forest. The georeferenced point cloud can be used in a similar manner as autonomous cars use HD (high-definition) maps for absolute positioning (see Levinson et al., 2007). Since GNSS (Global Navigation Satellite System) visibility is unobstructed above the canopy, the HD map (point cloud) will be positionally accurate. When approaching lower levels of the canopy, the position is determined by matching lidar returns with respect to the HD point cloud by applying e.g. Iterative Closest Points (ICP) variants (Rusinkiewicz and Levoy, 2001; Censi, 2008; Jež, 2008; Hong et al., 2010). The localization accuracy is related to the grid size of the HD map. Since the HD map easily includes hundreds of millions of points even for short ranges, different variants have been developed (Javanmardi et al., 2018). Tu et al. (2016) compressed the point cloud applying image compression techniques. Biber and Straßer (2003) represented the environment by normal distributions (NDT) instead of the raw point cloud. Magnusson et al. (2007) extended the NDT idea to the 3D. The HD map can be updated when approaching the lower levels of

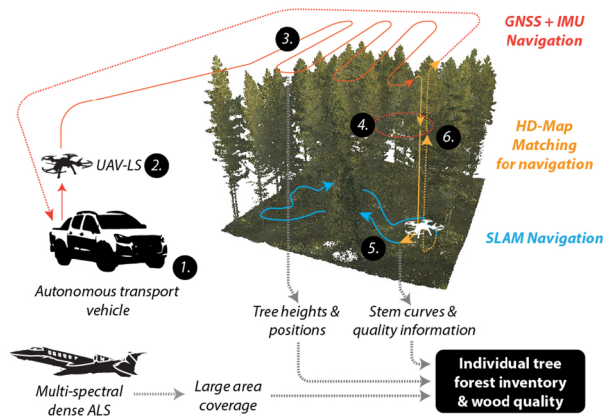


**Fig. 16.** The robotic-assisted end-to-end concept, for which the current study offers one practical application. The mini-UAV (2) departs from the car (1), and navigates itself to the forest area where high-quality reference measurements are needed. With the help of GNSS and IMU integration (3) and using the 3D point cloud (HD map, 4), a possible fly-through area is calculated and the mini-UAV flies to under-canopy (6). When the UAV reaches a height between 2–6 m (above the ground level), it starts to fly horizontally (5) in order to map as large an area as possible.

the canopy according to the concepts described in Jo et al. (2018). Then, the scanner is adjusted to a forward-looking mode and under-canopy flying is carried out using the principles following Vandapel et al. (2005). The under-canopy relative position of the scanner is then determined by SLAM (Simultaneous Localization and Mapping) and absolute position by matching the SLAM determined point cloud with the HD map. Recent developments in under canopy navigation include Higtuti et al. (2019), Schultz et al. (2016) and Cui et al. (2016).

The point cloud of the trees in the forest is then collected along the flight. Finally, the UAV continues to the next plot or to the car to be charged for deployment at the next plot after an autonomous drive. The post-processing depicted in this paper can be applied to derive stem characteristics. The concept requires a relatively good forest road network such as that available in Scandinavian forests. The concept can be used for automated field data collection supporting all kinds of earth observation applications.

## 6. Conclusions

Conventional manual forest plot measurements are implemented using calipers, measuring tapes and hypsometers leading to an accuracy ranging from 10% to 15% for the stem volume at individual tree level. This accuracy level has been reached with remote sensing techniques only when using multi-scan terrestrial laser scanning and the best state-of-the-art algorithms. In this paper, we showed that we can achieve the same accuracy by using a combination of under-canopy and above-canopy UAV laser scanning data.

In this study, the manually operated UAV, equipped with a Kaarta Stencil-1 laser scanner, provided a point cloud for two boreal forest test sites classified as sparse and obstructed. The point clouds collected with

the under-canopy flying UAV were used for stem curve estimation. The data processing work flow included a robust arc finding algorithm designed for point clouds collected with a 3D scanner, a post-SLAM arc matching algorithm and a PCA-based inclination angle correction. Using the proposed work flow, we were able to detect 93% of the stems in the sparse plot and 84% of the stems in the obstructed plot. Using the proposed work flow, the DBH was estimated with an RMSE of 2.2% in the sparse plot and with an RMSE of 3.1% in the obstructed plot, whereas the corresponding errors for the stem curve estimates were 5.0% and 5.2% on the two sites, respectively. Additionally, we collected point clouds of the two test sites using an above-canopy flying UAV in order to perform accurate tree height measurements that were required for stem volume estimation. By utilizing the extracted stem curves and tree heights, we were able to estimate the stem volumes for individual trees with an RMSE of 10% in both of the plots without using any allometric models.

Our results imply that under-canopy UAV laser scanning has great potential for realizing fast and accurate field reference data collection. The results were the best for pine trees with a detection rate of 100% and a stem volume estimation error below 10%. Future studies should focus on spruces and dense, complex canopies in order to be able to reach practical performance for field inventories. Developments in SLAM algorithms, autonomous UAV navigation and collision avoidance are also needed. Besides the application depicted in this paper, the robotic-assisted end-to-end approach envisioned for the future could provide extensive possibilities to automated field data collection supporting all kinds of earth observation applications.

## Acknowledgements

We gratefully acknowledge Academy of Finland and Strategic Research Council that funded this research through grants “Centre of Excellence in Laser Scanning Research (CoE-LaSR) (Academy decision 307362)”, “Estimating Forest Resources and Quality-related Attributes Using Automated Methods and Technologies” (Academy decision 334830) and “Competence-Based Growth Through Integrated Disruptive Technologies of 3D Digitalization, Robotics, Geospatial Information and Image Processing/Computing – Point Cloud Ecosystem (293389/ 314312)”. We would also like to thank the reviewers for their constructive comments that helped us improve the manuscript.

Author contributions: E.H. acted as the sole first author and created all the algorithms, processed the data to obtain the results and wrote the majority of the article. T.H. and H.K. planned and carried out the UAV data measurements. J.H. and H.K. acted as senior authors. J.H. made the experimental plan, provided basic concepts for data processing, and complemented in writing of the paper. E.H. and J.H. collected field reference data in 2019 needed for growth compensation. M.W. and J.W. provided insights throughout the paper, and improved the manuscript. J.P. processed the field reference stem curves. J-P.V. and E.H. drafted the images. O.P. provided mathematical matching algorithm to match the under-canopy and above-canopy point clouds and to convert SLAM point clouds into the global coordinate system. Others participated in improving the manuscript.

## Appendix A. Sensitivity analysis of the stem curve extraction algorithm

In this section, we present a simple sensitivity analysis for the stem curve extraction algorithm (see Section 3.2) with the goal to show that the results provided by the algorithm are not sensitive to small changes in the parameter values. Note also that the parameter values provided in Section 3 were chosen heuristically. As a result, some of the modified parameter values resulted in even lower errors than those presented in Section 4. However, one should bear in mind that the best results obtained as a result of a parameter sweep can exhibit over-fitting.

In Table A.4, we show the results of stem detection, DBH estimation, stem curve estimation and stem volume estimation when the parameter values were varied one at a time. Note that we varied only such parameter values whose effect we presumed to be the most significant for the algorithm. Based on the table, we can note that the results hardly changed even though some of the parameters were changed by large relative amounts. As an overall trend, we can observe that the errors decreased when the quality criteria ( $N_{\min}$ ,  $\sigma_R$ ,  $\sigma_{\min}$  etc) for the arcs were made stricter. However, making the quality criteria too strict reduced the completeness of stem detection, especially, when it comes to the two spruces detected in

**Table A.4**

Sensitivity analysis for the stem curve extraction algorithm described in Section 3.2. The parameters are varied one at a time, and the results obtained by using the modified parameter values are listed in the table. The default parameter value is shown in parentheses after the modified value.

Parameters	Stem detection		DBH		Stem curve		Stem volume	
	Completeness (%)	Correctness (%)	Bias-%	RMSE-%	Bias-%	RMSE-%	Bias-%	RMSE-%
Default								
Sparse plot	93%	100%	1.1%	2.2%	1.8%	5.0%	3.8%	10.1%
Obstructed plot	84%	100%	1.0%	3.1%	2.0%	5.2%	3.7%	10.1%
Inlier threshold (RANSAC) $d_{in} = 2$ cm (3 cm)								
Sparse plot	93%	100%	1.1%	2.0%	1.3%	4.8%	2.6%	10.1%
Obstructed plot	81%	100%	0.3%	3.2%	1.6%	3.9%	1.1%	5.8%
Inlier threshold (RANSAC) $d_{in} = 4$ cm (3 cm)								
Sparse plot	93%	100%	1.4%	2.4%	2.3%	5.5%	5.6%	11.5%
Obstructed plot	84%	100%	0.6%	4.0%	2.5%	5.5%	5.3%	15.5%
Point number threshold $N_{min} = 30$ (50)								
Sparse plot	93%	100%	1.5%	2.5%	2.6%	5.7%	5.9%	11.0%
Obstructed plot	84%	100%	0.3%	3.6%	2.7%	5.7%	5.4%	10.7%
Point number threshold $N_{min} = 70$ (50)								
Sparse plot	93%	100%	0.9%	2.0%	1.2%	4.6%	2.1%	9.8%
Obstructed plot	84%	100%	0.5%	4.0%	1.6%	4.2%	0.9%	7.6%
Radial residual threshold $\sigma_R = 1.2$ cm (1.5 cm)								
Sparse plot	93%	100%	1.1%	2.4%	1.8%	5.0%	4.0%	10.5%
Obstructed plot	81%	100%	0.6%	3.2%	2.2%	4.3%	1.7%	6.9%
Radial residual threshold $\sigma_R = 2.0$ cm (1.5 cm)								
Sparse plot	93%	100%	1.1%	2.2%	1.9%	5.0%	4.4%	10.7%
Obstructed plot	84%	100%	0.6%	4.3%	2.0%	5.2%	4.4%	11.8%
Max. angle between points $\Delta\theta_{max} = 7^\circ$ ( $10^\circ$ )								
Sparse plot	93%	100%	0.4%	2.0%	0.6%	4.6%	0.3%	9.5%
Obstructed plot	84%	100%	0.2%	3.3%	1.0%	3.8%	-0.1%	8.5%
Max. angle between points $\Delta\theta_{max} = 20^\circ$ ( $10^\circ$ )								
Sparse plot	93%	100%	1.8%	3.3%	3.1%	6.3%	7.7%	13.0%
Obstructed plot	86%	100%	0.6%	3.3%	2.9%	5.7%	5.8%	10.7%
Min. inlier ratio (RANSAC) $\eta_{in} = 0.6$ (0.7)								
Sparse plot	93%	98%	1.4%	2.5%	2.1%	5.2%	4.9%	10.9%
Obstructed plot	86%	100%	0.6%	3.7%	2.4%	5.3%	4.1%	9.8%
Min. inlier ratio (RANSAC) $\eta_{in} = 0.8$ (0.7)								
Sparse plot	93%	100%	1.0%	1.9%	1.7%	5.0%	4.1%	10.6%
Obstructed plot	84%	100%	0.3%	3.7%	0.2%	4.6%	2.4%	8.0%
DBSCAN $minPts_2 = 15$ (5)								
Sparse plot	93%	100%	1.0%	1.9%	1.8%	4.9%	4.4%	10.5%
Obstructed plot	81%	100%	0.4%	3.4%	2.5%	5.3%	3.7%	9.7%
DBSCAN $minPts_2 = 50$ (5)								
Sparse plot	93%	100%	1.2%	2.2%	1.7%	5.0%	3.9%	10.6%
Obstructed plot	79%	100%	0.2%	3.6%	2.3%	5.1%	4.3%	12.5%
Min. angle of arc $\theta_{min} = 90^\circ$ ( $108^\circ$ )								
Sparse plot	93%	100%	1.1%	2.1%	2.2%	5.3%	4.9%	11.0%
Obstructed plot	84%	100%	0.7%	3.7%	2.4%	5.8%	5.2%	15.8%
Min. angle of arc $\theta_{min} = 126^\circ$ ( $108^\circ$ )								
Sparse plot	93%	100%	1.1%	2.3%	1.7%	5.0%	3.4%	10.3%
Obstructed plot	84%	100%	0.4%	2.6%	1.5%	4.7%	2.2%	8.6%

the obstructed test site. Additionally, we can note that the relative changes in the results were more pronounced for the obstructed plot. One major reason for this observation is the fact that the large birch depicted in Fig. 12 has a large volume ( $3.3 \text{ m}^3$ ) as compared with the other trees on the obstructed plot (average  $0.86 \text{ m}^3$ ). Therefore, the modeling accuracy of the large birch had a relatively large impact on the results of the whole plot. Making the quality criteria less strict resulted in an over-estimation of the diameter of the large birch at heights around  $z = 5$  m, which, in turn, reduced the accuracy of stem volume estimation.

Note also that we obtained less than 50 good quality arcs for the two spruces detected in the obstructed plot, and therefore the minimum number of arcs required for stem detection ( $minPts_2$ ) should not be set too high if the spruces are to be detected. To detect the spruce illustrated in Fig. 13, the parameter  $minPts_2$  should have a value below 15 since the occlusion of the stem greatly limits the number of extracted arcs.

As a final note, the value of the parameter  $\Delta\theta_{\min}$  had a relatively large impact on the bias of the stem curve and volume estimation since it controls how easily points close to the boundaries of an arc are removed. If the value of  $\Delta\theta_{\min}$  was set to a large value, the outlier filtering did not work efficiently, which increased the risk of diameter over-estimation due to the noise points close to the edges of arcs.

## References

- Al-Sharadqah, A., Chernov, N., 2009. Error analysis for circle fitting algorithms. *Electron. J. Stat.* 3, 886–911.
- Bauwens, S., Bartholomeus, H., Calders, K., Lejeune, P., 2016. Forest inventory with terrestrial lidar: a comparison of static and hand-held mobile laser scanning. *Forests* 7 (6), 127.
- Biber, P., Straßer, W., 2003. The normal distributions transform: a new approach to laser scan matching. In: *Proceedings 2003 IEEE/RSJ International Conference on Intelligent Robots and Systems (IROS 2003)* (Cat. No. 03CH37453), vol. 3. IEEE, pp. 2743–2748.
- Bienert, A., Georgi, L., Kunz, M., Maas, H.-G., von Oheimb, G., 2018. Comparison and combination of mobile and terrestrial laser scanning for natural forest inventories. *Forests* 9 (7), 395.
- Brede, B., Lau, A., Bartholomeus, H., Kooistra, L., 2017. Comparing Riegl RiCOPTER UAV LiDAR derived canopy height and DBH with terrestrial lidar. *Sensors* 17 (10), 2371.
- Cabo, C., Del Pozo, S., Rodríguez-González, P., Ordóñez, C., González-Aguilera, D., 2018. Comparing terrestrial laser scanning (TLS) and wearable laser scanning (WLS) for individual tree modeling at plot level. *Remote Sens.* 10 (4), 540.
- Censi, A., 2008. An ICP variant using a point-to-line metric. In: *2008 IEEE International Conference on Robotics and Automation*. IEEE, pp. 19–25.
- Čerňava, J., Mokroš, M., Tuček, J., Antal, M., Slatkovská, Z., 2019. Processing chain for estimation of tree diameter from GNSS-IMU-based mobile laser scanning data. *Remote Sens.* 11 (6), 615.
- Chisholm, R.A., Cui, J., Lum, S.K., Chen, B.M., 2013. UAV lidar for below-canopy forest surveys. *J. Unmanned Veh. Syst.* 1 (1), 61–68.
- Cui, J.Q., Lai, S., Dong, X., Chen, B.M., 2016. Autonomous navigation of UAV in foliage environment. *J. Intell. Robot. Syst.* 84 (1–4), 259–276.
- De Boor, C., De Boor, C., Mathématique, E.-U., De Boor, C., De Boor, C., 1978. *A practical guide to splines*. Vol. 27 Springer-verlag, New York.
- Del Perugia, B., Giannetti, F., Chirici, G., Travaglini, D., 2019. Influence of scan density on the estimation of single-tree attributes by hand-held mobile laser scanning. *Forests* 10 (3), 277.
- Ester, M., Kriegel, H.-P., Sander, J., Xu, X., 1996. A density-based algorithm for discovering clusters in large spatial databases with noise. In: *Kdd 96*, 226–231.
- Fan, Y., Feng, Z., Mannan, A., Khan, T., Shen, C., Saeed, S., 2018. Estimating tree position, diameter at breast height, and tree height in real-time using a mobile phone with RGB-D slam. *Remote Sens.* 10 (11), 1845.
- Fischler, M.A., Bolles, R.C., 1981. Random sample consensus: a paradigm for model fitting with applications to image analysis and automated cartography. *Commun. ACM* 24 (6), 381–395.
- Forsman, M., Börlin, N., Olofsson, K., Reese, H., Holmgren, J., 2018. Bias of cylinder diameter estimation from ground-based laser scanners with different beam widths: a simulation study. *ISPRS J. Photogramm. Remote Sens.* 135, 84–92.
- Forsman, M., Holmgren, J., Olofsson, K., 2016. Tree stem diameter estimation from mobile laser scanning using line-wise intensity-based clustering. *Forests* 7 (9), 206.
- Harikumar, A., Bovolo, F., Bruzzone, L., 2017. An approach to conifer stem localization and modeling in high density airborne lidar data. In: *Image and Signal Processing for Remote Sensing XXIII*. Vol. 10427. International Society for Optics and Photonics, p. 104270Q.
- Higuti, V.A., Velasquez, A.E., Magalhaes, D.V., Becker, M., Chowdhary, G., 2019. Under canopy light detection and ranging-based autonomous navigation. *J. Field Robot.* 36 (3), 547–567.
- Holmgren, J., Tulldahl, M., Nordlöf, J., Willén, E., Olsson, H., 2019. Mobile laser scanning for estimating tree stem diameter using segmentation and tree spine calibration. *Remote Sens.* 11 (23), 2781.
- Hong, S., Ko, H., Kim, J., 2010. VICP: Velocity updating iterative closest point algorithm. In: *2010 IEEE International Conference on Robotics and Automation*. IEEE, pp. 1893–1898.
- Hyypä, J., Kelle, O., Lehikoinen, M., Inkinen, M., 2001. A segmentation-based method to retrieve stem volume estimates from 3-D tree height models produced by laser scanners. *IEEE Trans. Geosci. Remote Sens.* 39 (5), 969–975.
- Hyypä, E., Kukko, A., Kajaluoto, R., White, J.C., Wulder, M.A., Pyörälä, J., Liang, X., Yu, X., Wang, Y., Kaartinen, H., et al., 2020. Accurate derivation of stem curve and volume using backpack mobile laser scanning. *ISPRS J. Photogramm. Remote Sens.* 161, 246–262.
- Hyypä, J., Virtanen, J.-P., Jaakkola, A., Yu, X., Hyypä, H., Liang, X., 2017. Feasibility of Google Tango and Kinect for crowdsourcing forestry information. *Forests* 9 (1), 6.
- Ighhaut, J., Cabo, C., Puliti, S., Piermattei, L., O'Connor, J., Rosette, J., 2019. Structure from motion photogrammetry in forestry: a review. *Curr. Forest. Rep.* 5 (3), 155–168.
- Jaakkola, A., Hyypä, J., Kukko, A., Yu, X., Kaartinen, H., Lehtomäki, M., Lin, Y., 2010. A low-cost multi-sensoral mobile mapping system and its feasibility for tree measurements. *ISPRS J. Photogramm. Remote Sens.* 65 (6), 514–522.
- Jaakkola, A., Hyypä, J., Yu, X., Kukko, A., Kaartinen, H., Liang, X., Hyypä, H., Wang, Y., 2017. Autonomous collection of forest field reference the outlook and a first step with UAV laser scanning. *Remote Sens.* 9 (8), 785.
- Javanmardi, E., Javanmardi, M., Gu, Y., Kamijo, S., 2018. Factors to evaluate capability of map for vehicle localization. *IEEE Access* 6, 49850–49867.
- Jež, O., 2008. 3D mapping and localization using leveled map accelerated ICP. In: *European Robotics Symposium 2008*. Springer, pp. 343–353.
- Jo, K., Kim, C., Sunwoo, M., 2018. Simultaneous localization and map change update for the high definition map-based autonomous driving car. *Sensors* 18 (9), 3145.
- Kukko, A., Kajaluoto, R., Kaartinen, H., Lehtola, V.V., Jaakkola, A., Hyypä, J., 2017. Graph SLAM correction for single scanner MLS forest data under boreal forest canopy. *ISPRS J. Photogramm. Remote Sens.* 132, 199–209.
- Levinson, J., Montemerlo, M., Thrun, S., 2007. Map-based precision vehicle localization in urban environments. In: *Robotics: Science and Systems*. Vol. 4. Citeseer, p. 1.
- Liang, X., Hyypä, J., Kaartinen, H., Lehtomäki, M., Pyörälä, J., Pfeifer, N., Holopainen, M., Brolly, G., Francesco, P., Hackenberg, J., et al., 2018a. International benchmarking of terrestrial laser scanning approaches for forest inventories. *ISPRS J. Photogramm. Remote Sens.* 144, 137–179.
- Liang, X., Hyypä, J., Kukko, A., Kaartinen, H., Jaakkola, A., Yu, X., 2014a. The use of a mobile laser scanning system for mapping large forest plots. *IEEE Geosci. Remote Sens. Lett.* 11 (9), 1504–1508.
- Liang, X., Kankare, V., Yu, X., Hyypä, J., Holopainen, M., 2014b. Automated stem curve measurement using terrestrial laser scanning. *IEEE Trans. Geosci. Remote Sens.* 52 (3), 1739–1748.
- Liang, X., Kukko, A., Hyypä, J., Lehtomäki, M., Pyörälä, J., Yu, X., Kaartinen, H., Jaakkola, A., Wang, Y., 2018b. In-situ measurements from mobile platforms: an emerging approach to address the old challenges associated with forest inventories. *ISPRS J. Photogramm. Remote Sens.* 143, 97–107.
- Liang, X., Kukko, A., Kaartinen, H., Hyypä, J., Yu, X., Jaakkola, A., Wang, Y., 2014c. Possibilities of a personal laser scanning system for forest mapping and ecosystem services. *Sensors* 14 (1), 1228–1248.
- Liang, X., Litkey, P., Hyypä, J., Kaartinen, H., Vastaranta, M., Holopainen, M., 2012. Automatic stem mapping using single-scan terrestrial laser scanning. *IEEE Trans. Geosci. Remote Sens.* 50 (2), 661–670.
- Liang, X., Wang, Y., Pyörälä, J., Lehtomäki, M., Yu, X., Kaartinen, H., Kukko, A., Honkavaara, E., Issaoui, A.E., Nevalainen, O., et al., 2019. Forest in situ observations using unmanned aerial vehicle as an alternative of terrestrial measurements. *Forest Ecosyst.* 6 (1), 20.
- Lindström, H., 2007. Basic density of norway spruce. Part II. Predicted by stem taper, mean growth ring width, and factors related to crown development. *Wood Fiber Sci.* 28 (2), 240–251.
- Luoma, V., Saarinen, N., Kankare, V., Tanhuanpää, T., Kaartinen, H., Kukko, A., Holopainen, M., Hyypä, J., Vastaranta, M., 2019. Examining changes in stem taper and volume growth with two-date 3d point clouds. *Forests* 10 (5), 382.
- Luoma, V., Saarinen, N., Wulder, M.A., White, J.C., Vastaranta, M., Holopainen, M., Hyypä, J., 2017. Assessing precision in conventional field measurements of individual tree attributes. *Forests* 8 (2), 38.
- Magnusson, M., Lilienthal, A., Duckett, T., 2007. Scan registration for autonomous mining vehicles using 3D-NDT. *J. Field Robot.* 24 (10), 803–827.
- Marselis, S.M., Yebra, M., Jovanovic, T., van Dijk, A.I., 2016. Deriving comprehensive forest structure information from mobile laser scanning observations using automated point cloud classification. *Environ. Modell. Softw.* 82, 142–151.
- Pierzchała, M., Giguère, P., Astrup, R., 2018. Mapping forests using an unmanned ground vehicle with 3D lidar and graph-SLAM. *Comput. Electron. Agric.* 145, 217–225.
- Pollock, D., et al., 1993. *Smoothing with cubic splines*.
- Qian, C., Liu, H., Tang, J., Chen, Y., Kaartinen, H., Kukko, A., Zhu, L., Liang, X., Chen, L., Hyypä, J., 2017. An integrated GNSS/INS/LiDAR-SLAM positioning method for highly accurate forest stem mapping. *Remote Sens.* 9 (1), 3.
- Rusinkiewicz, S., Levoy, M., 2001. Efficient variants of the ICP algorithm. In: *3DIM*. Vol. 1. pp. 145–152.
- Schultz, A., Gilabert, R., Bharadwaj, A., de Haag, M.U., Zhu, Z., 2016. A navigation and mapping method for UAS during under-the-canopy forest operations. *IEEE*, pp. 739–746.
- Tang, J., Chen, Y., Kukko, A., Kaartinen, H., Jaakkola, A., Khoramshahi, E., Hakala, T., Hyypä, J., Holopainen, M., Hyypä, H., 2015. SLAM-aided stem mapping for forest inventory with small-footprint mobile lidar. *Forests* 6 (12), 4588–4606.
- Tomaščík, J., Saloň, Š., Tunák, D., Chudý, F., Kardoš, M., 2017. Tango in forests – an initial experience of the use of the new Google technology in connection with forest inventory tasks. *Comput. Electron. Agric.* 141, 109–117.
- Tu, C., Takeuchi, E., Miyajima, C., Takeda, K., 2016. Compressing continuous point cloud data using image compression methods. In: *2016 IEEE 19th International Conference on Intelligent Transportation Systems (ITSC)*. IEEE, pp. 1712–1719.
- Vandapel, N., Kuffner, J., Amidi, O., 2005. Planning 3-D path networks in unstructured environments. In: *Proceedings of the 2005 IEEE International Conference on Robotics and Automation*. IEEE, pp. 4624–4629.
- Vian, J.L., Przybylko, J., 2012. Tree metrology system. US Patent 9,198,363.

- Wallace, L., Lucieer, A., Watson, C., Turner, D., 2012. Development of a UAV-lidar system with application to forest inventory. *Remote Sens.* 4 (6), 1519–1543.
- Wallace, L., Musk, R., Lucieer, A., 2014. An assessment of the repeatability of automatic forest inventory metrics derived from UAV-borne laser scanning data. *IEEE Trans. Geosci. Remote Sens.* 52 (11), 7160–7169.
- Wang, Y., Lehtomäki, M., Liang, X., Pyörälä, J., Kukko, A., Jaakkola, A., Liu, J., Feng, Z., Chen, R., Hyypä, J., 2019a. Is field-measured tree height as reliable as believed—a comparison study of tree height estimates from field measurement, airborne laser scanning and terrestrial laser scanning in a boreal forest. *ISPRS J. Photogramm. Remote Sens.* 147, 132–145.
- Wang, Y., Pyörälä, J., Liang, X., Lehtomäki, M., Kukko, A., Yu, X., Kaartinen, H., Hyypä, J., 2019b. In situ biomass estimation at tree and plot levels: What did data record and what did algorithms derive from terrestrial and aerial point clouds in boreal forest. *Remote Sens. Environ.* 232, 111309.
- Wieser, M., Mandlbürger, G., Hollaus, M., Otepka, J., Glira, P., Pfeifer, N., 2017. A case study of UAS-borne laser scanning for measurement of tree stem diameter. *Remote Sens.* 9 (11), 1154.